As originally published in the SMTA Proceedings.

The Effect of Thermal Cycling Profile on Thermal Fatigue Performance of a 192-Pin Chip Array BGA with Hybrid, Homogeneous, and Resin Reinforced Low Temperature Solder Interconnects

Dan Burkholder[1], Russ Brown[2], Jagadeesh Radhakrishnan[2], Pubudu Goonetilleke[3], Raiyo Aspandiar[3], Yunfei Wang[3], Richard Coyle[4], Faramarz Hadian[5], Babak Arfaei[5], Vasu Vasudevan[6], Aileen Allen[7], Keith Howell[8], Qin Chen[9], Derek Daily[10], Haley Fu[11], Carol Handwerker[12], Ralph Lauwaert[13], Daniel Werkhoven[13], Kei Murayama[14], Hongwen Zhang[15], Francis Mutuku[15], Huaguang Wang[15], Morgana Ribas[16], and Murali Sarangapani[17]

[1]Intel Corporation, Chandler, AZ, USA, [2]Intel Corporation, Folsom, CA, USA, [3]Intel Corporation, Hillsboro, OR, USA, [4]Nokia, Murray Hill, NJ, USA, [5]Physics Dept., SUNY-Binghamton, Binghamton, NY, USA, [6]Dell Technologies, Round Rock, TX, USA, [7]HP, Inc., Palo Alto, CA, USA, [8]Nihon Superior Co., Ltd., Osaka, Japan, [9]Eunow, Suzhou, China, [10]Senju Comtek Corp, Santa Clara, CA, [11]iNEMI, Shanghai, China, [12]Purdue University, West Lafayette, IN, USA, [13]Interflux Electronic nv, Belgium, [14]Shinko Electric Industries Co. LTD., Nagano, Japan, [15]Indium Corporation, Clinton, NY, USA, [16]MacDermid Alpha Electronics Solutions, Bengaluru, India, [17]Heraeus Materials Singapore Pte Ltd, Singapore

dan.s.burkholder@intel.com

ABSTRACT

There is an increasing interest in many market segments to use solder alloys with lower melting temperatures for electronics assembly. Low temperature solders can provide manufacturing, economic, and environmental benefits. Since 2015, the International Electronics Manufacturing Initiative (iNEMI) Low Temperature Solder Process and Reliability (LTSPR) Project has been evaluating Low Temperature Solder (LTS) paste formulations based on the Bi-Sn system. This paper summarizes the findings from a thermal cycling test to evaluate the effect of thermal cycling profile on thermal fatigue performance of low temperature solders.

The study uses a daisy chained printed circuit board and two daisy chained ball grid array (BGA) test vehicles, a 192-pin chip array BGA (CABGA192) and an 84-pin thin core BGA (CTBGA84). The test matrix includes multiple LTS solder alloys designated by code names. The alloys are down selected from the larger project alloy matrix based on assembly effectiveness and mechanical test performance. There are two types of solder alloys, so-called ductile metallurgies that employ alloy modifications to improve the properties of the basic Bi-Sn alloy, and joint reinforced pastes (JRP) that employ resin additions that generate in situ filets during reflow to provide joint support. Components manufactured with the established SAC305 (Sn3.0Ag0.5Cu) composition are used as the baseline for the study.

Three types of LTS solder joints are evaluated, homogeneous, hybrid (heterogeneous), and hybrid formed with joint reinforced pastes (JRP). Hybrid joints have a SAC BGA soldered with a ductile metallurgy LTS solder paste. The resultant solder joint consists of an unmelted SAC region at the package side of the joint and a melted region at the PCB side containing Bi from the solder paste. A hybrid joint also may be described as heterogeneous because it contains two regions with clearly distinct microstructures, compositions, and properties. Homogeneous joints are created when a BGA manufactured with LTS solder spheres is soldered to the PCB using a LTS solder paste with matching composition. A JRP joint is a special type of hybrid joint that has resin filets that form during reflow to enhance joint support.

The test plan includes two distinct Accelerated Temperature Cycling (ATC) profiles, 0/100 °C (IPC-9701B, TC1) and -15/85 °C (selected due to the homologous temperature comparison between Sn-Ag-Cu and Bi-Sn solder), using the CABGA192 BGA component. This report includes the temperature cycling results for 7 experimental legs of the CABGA192 BGA component (Table 2) tested with the -15/85 °C profile compared to the results of the 0/100 °C profile (presented in a previous publication [37]). Weibull statistics, microstructural characterization, and failure mode analysis are used to compare the differences in alloy performance and to compare the performance of hybrid and homogeneous solder joint configurations.

Failure analysis from both ATC profiles showed that most of the solder joints failed due to fatigue cracking within the bulk solder near the package side, regardless of alloy composition, joint construction (hybrid, homogeneous, or hybrid JRP), and package type.

The CABGA192 component was affected differently across the 0/100 °C and -15/85 °C thermal cycling profiles. From a characteristic lifetime analysis, all of the low temperature solder test legs, across both ATC profiles, were shown to have a characteristic lifetime performance equivalent to the SAC baseline, with one exception; the homogeneous Red Flesh leg as run in the 0/100 °C profile. However, this performance delta went away when this leg was run in the less aggressive -15/85 °C profile. When looking at the thermal cycle profile ratio comparisons for characteristic lifetime, all test legs were extended beyond the SAC baseline in the less aggressive -15/85 °C profile, except for the Hybrid Sultan 2 and the Golden Pillow 2 JRP, which showed a decrease in the ratio.

From a 1% cumulative failure analysis, the homogeneous Red Flesh and homogeneous Sultan 2 were shown to have relatively lower performance as compared with the SAC305 baseline in the 0/100 °C profile. However, this performance delta went away when these legs were run in the less aggressive -15/85 °C profile. It was also observed that for both the Beserah JRP and Golden Pillow 2 JRP as run in the less aggressive -15/85 °C profile, there was relatively lower 1% cumulative failure as compared to both the 0/100 °C profile and to the SAC305 baseline. This finding was also observed when looking at the thermal cycle profile ratio comparisons for 1% cumulative failure, which suggests that JRP resins may have a sensitivity to the colder accelerated temperatures as were present in the -15/85 °C profile.

Key words: Low temperature solder, thermal fatigue reliability, thermal cycling, accelerated temperature cycling, hybrid solder joints, homogeneous solder joints, joint reinforced solder pastes, resin, bismuth, solder ball drift.

INTRODUCTION

Low Temperature Solder

The development and implementation of Low Temperature Solders (LTS) for electronic assembly is being driven by technical, economic, and environmental requirements. A notable motivation for implementing low temperature solder processes is to minimize dynamic warpage (flatness as a function of temperature) of ball grid array (BGA) components and printed circuit boards. Warpage during solder reflow can reduce assembly yields and result in unpredictable early field failures by creating defects such as head on pillow (HoP), Non-Wet Open (NWO), and solder ball bridging (SBB) [1]. Aspandiar et al. [2] and Mokler et al. [3] have presented data that suggest component warpage could be minimized if reflow is performed in the range of 160 to 180 °C. This temperature range is well-below the current Sn-Ag-Cu (SAC) reflow range of 240-260 °C. The Mokler study shows a 30-50 % reduction in warpage in a flip chip BGA (FCBGA) when reflowed below 180 °C. However, replacing the current SAC alloys with low temperature solders requires improving the mechanical reliability performance and characterizing thermal fatigue performance of low temperature solders. Additionally, assembly processes may need to be created or adapted to support implementation of these alloys.

Low temperature soldering, in the context of these current industry discussions, refers to reflow at a peak temperature below 200 °C. The leading solder alloy candidates for reflow below 200 ºC are based on the Bi-Sn binary alloy system that has a melting point of 138 ºC at its eutectic composition of approximately 42 wt.% Sn and 58 wt.% Bi [4]. The metallurgy and technology of low temperature solder alloys is evolving rapidly and detailed information on solder assembly processing, alloy development, and reliability testing can be found in several comprehensive reviews [5-10]. The 42Sn-58Bi binary eutectic alloy initially was considered a viable Pb-free candidate to replace Sn-Pb solder, so there are already many available reports on its performance [11-15]. However, independent investigations confirmed the poor mechanical shock resistance [16] and lower fatigue life [14] of 42Sn-58Bi, which was attributed to its brittle two-phase lamellar microstructure.

Since those earlier evaluations of the 42Sn-58Bi binary eutectic alloy, solder suppliers have developed new low temperature solder pastes to improve the reliability limitations of the binary 42Sn-58Bi alloy. For example, the ductility of the Bi-Sn alloy can be enhanced by incorporating elemental additions that promote grain refinement, precipitate hardening or solid solution strengthening [3]. In this way, the Bi-Sn microstructure is modified to combine its inherent mechanical strength with better ductility and fatigue resistance to withstand mechanical stresses due to shock or cyclic stresses, such as those associated with mechanical shock or thermal cycling, respectively. LTS alloys with enhanced properties due to elemental additions often are referred to as ductile metallurgies. Another option is the reinforcement of the solder joint by incorporating resin in the solder paste. In this case, the resins contained in the solder paste cure during the reflow, forming a physical reinforcement layer that acts as a mechanical barrier around the metallic solder joint [17]. LTS alloys with enhanced properties due to resin additions are referred to as joint reinforced pastes (JRP).

The primary focus of recent industry LTS studies is on the assembly and reliability challenges of hybrid (sometimes called heterogeneous, or mixed metallurgy) ball grid array (BGA) solder joints. A hybrid LTS solder joint is defined as a SAC BGA that is reflow assembled with LTS solder paste. LTS hybrid BGA solder joints consist of an upper region of

unmelted SAC solder and a lower region of melted SAC solder mixed with the Bi-Sn solder paste. Figure 1 shows a back scattered electron (BSE) image of a hybrid solder joint. The Bi presents as the bright white phase in the backscattered imaging mode. Independent evaluations of Bi-Sn solders with ductile alloying or resin reinforcement have demonstrated promising results resisting mechanical shock [3, 18, 19] and thermal fatigue [20] in hybrid SAC-BiSn BGA assemblies.

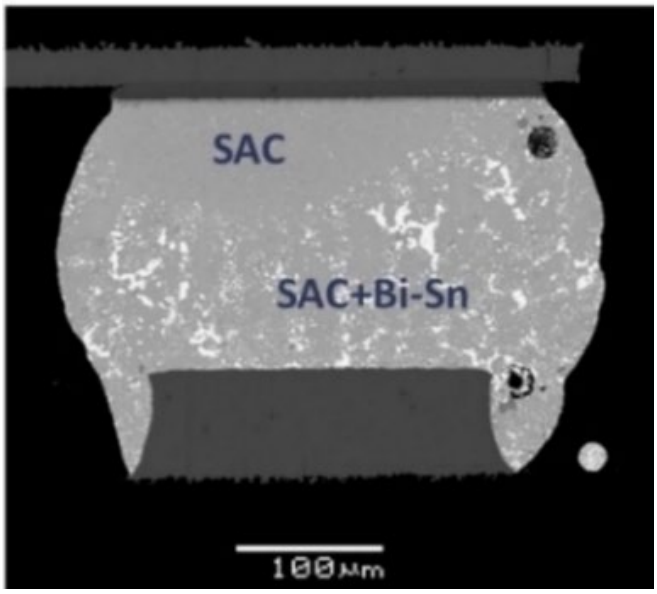

Figure 1. A cross-sectional back scattered scanning electron image of a hybrid or heterogenous ball grid array solder joint (figure published previously [37]).

The initial applications for low temperature solder have been in portable consumer electronics such as laptop computers [21], thus most of the hybrid reliability testing has been focused on mechanical shock and drop requirements [18, 19, 22-27]. However, some applications also require acceptable thermal fatigue reliability, and there are much fewer thermal cycling studies compared to drop/shock studies. Existing data are limited in scope, mostly due to the large number of variables under consideration such as solder processing parameters, alloy compositions, paste formulations, and component type [1, 9, 20, 23, 28, 29]. Despite more recent thermal cycling activity [30-34], many gaps remain in thermal fatigue data for hybrid solder joints.

To address the resources required for an unbiased and comprehensive evaluation of low temperature solder technology, the International Electronic Manufacturing Initiative (iNEMI) launched the BiSn-based Low Temperature Soldering Process and Reliability (LTSPR) Project in 2015. The project is supported by multiple stakeholders, including a diverse mix of Original Design Manufacturers (ODMs), Original Equipment Manufacturers (OEMs), Electronic Manufacturing Services (EMS), material suppliers, and universities. The first two phases of the project explored material selection, development, and optimization of surface mount processes specific to low temperature solders, and evaluation of mechanical shock performance [22, 24, 26, 27, 35, 36]. The project is currently in its third phase, which is evaluation of thermal cycling performance.

The iNEMI LTSPR thermal cycling test matrix includes multiple LTS solder alloys that were down selected from the first two phases based on assembly effectiveness and mechanical test performance. These alloys include the ductile metallurgies that employ alloy modifications to improve the properties of the basic Bi-Sn alloy, and joint reinforced pastes (JRP) that employ resin additions that generate in situ fillets during reflow to provide joint support. Components manufactured with the established SAC305 (Sn3.0Ag0.5Cu) composition are used as the control for the study.

In this third iNEMI LTSPR phase, testing is conducted with two distinct thermal cycling profiles, 0/100° C, and -15/85° C. This paper reports the thermal cycling results for the 192 I/O chip array ball grid array component (CABGA192) tested with the -15/85° C profile, and compares these results (as a companion paper) to the CABGA192 tested with the 0/100° C profile, presented in a previous publication [37]. Thermal cycling data is reported for only the CABGA192 component due to the testing of the CTBGA84 had not yet concluded, for the -15/85° C thermal cycling profile, at the time of this writing. Weibull statistics, microstructural characterization, and failure mode analysis are used to compare the differences in alloy performance and to compare the performance of hybrid and homogeneous solder joint configurations.

EXPERIMENTAL

Test Vehicle

Component and Test Board Description

The components and printed circuit board (PCB) test vehicle was developed initially for the iNEMI Alloy Alternatives project [38]. The daisy chained CABGA192 and CTBGA84 components [39] are shown in Figure 2. The solder alloy spheres on both packages are SAC305. The PCB test vehicle is 2.36 mm (93 mils) thick, with a 6-layer construction and 16 sites for the CABGA192 and another 16 sites for the CTBGA84 as shown in Figure 3.

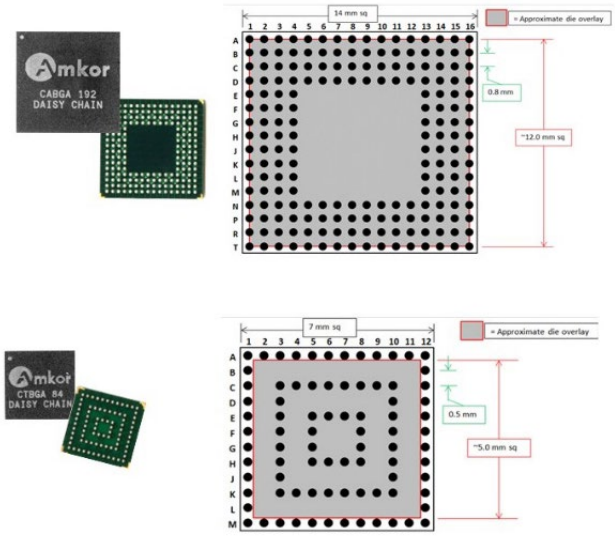

Figure 2. The CABGA192 and CTBGA84 daisy chained components and pin diagrams with die sizes and locations [37, 39].

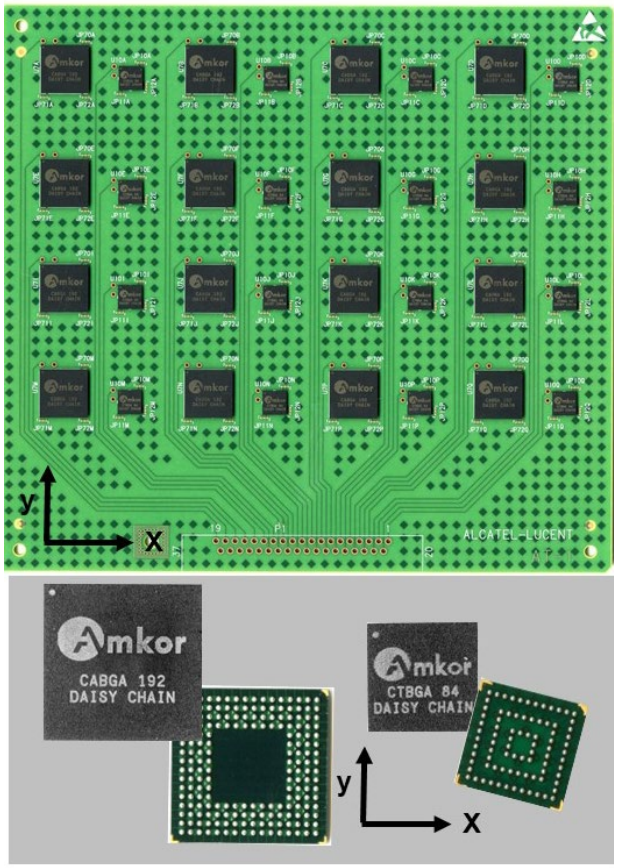

Figure 3. A fully populated, daisy chained PCB and the daisy chained CABGA192 and CTBGA84 components [37].

The boards were fabricated with Shengyi S7545 high temperature laminate material and an organic solderability preservative (OSP) final finish. The attributes of the components and PCB are provided in Table 1.

Table 1. BGA package and PCB attributes [37].

BGA Package Attributes		
Designation	CABGA192	CTBGA84
Die Size	12x12 mm	5x5 mm
Package Size	14x14 mm	7x7 mm
Ball Array	16x16	12x12
Ball Pitch	0.8 mm	0.5 mm
Ball Diameter	0.46 mm	0.3 mm
Pad Diameter	0.381 mm	0.3 mm
Pad Finish	Electrolytic Ni/Au	Electrolytic Ni/Au
Au thickness	0.6 µm	0.6 µm
PCB Attributes		
Dimensions	165 x 178 x 2.36 mm	
Laminate	Shengyi S7545	
Surface Finish	ENTEK Plus HT (OSP)	
No. Cu Layers	6	
Pad Diameter	0.356 mm	0.254 mm
Solder Mask Dia.	0.483 mm	0.381 mm
Glass Transition Temperature, T_g	146 °C (DSC) 168 °C (TMA)	
Decomposition Temperature, T_d	374 °C	

Board Assembly Parameters

Experimental Design

The experimental legs for the temperature cycling tests are listed in Table 2. The 7 legs include a SAC baseline for comparison, two of the best performing JRP solder pastes, Beserah and Golden Pillow 2, from the previous study [22] of mechanical shock drop reliability of a CPU BGA package, and two of the best ductile BiSn solder pastes, Red Flesh and Sultan 2, also from the previous CPU BGA package mechanical drop study [22]. The two ductile BiSn solder pastes were evaluated with both homogeneous and hybrid (heterogeneous) solder joints configurations. Results from all seven legs are included in this paper.

Table 2. The 7 Experimental Legs for the Temperature Cycling Tests [37].

Leg #	Leg Name	Component	Component Sphere Composition	Solder Paste Alloy	Solder Paste Category
1	SAC Baseline	CTBGA84 CABGA192	SAC305	SAC305	SAC Baseline
2	Beserah JRP	CTBGA84 CABGA192	SAC305	BiSn Eutectic	Joint Reinforced Paste (JRP)
3	Golden Pillow 2 JRP	CTBGA84 CABGA192	SAC305	BiSn + Microalloys	Joint Reinforced Paste (JRP)
4	Heterogeneous Red Flesh	CTBGA84 CABGA192	SAC305	BiSn + Microalloys	Ductile BiSn
5	Heterogeneous Sultan 2	CTBGA84 CABGA192	SAC305	BiSn + Microalloys	Ductile BiSn
6	Homogeneous Red Flesh	CTBGA84 CABGA192	Identical to Solder Paste	BiSn + Microalloys	Ductile BiSn
7	Homogeneous Sultan 2	CTBGA84 CABGA192	Identical to Solder Paste	BiSn + Microalloys	Ductile BiSn

Each Accelerated Temperature Cycling (ATC) test board contains 16 CABGA192 and 16 CTBGA84 components. Replicate test boards are used to achieve a sample size of 32 for each component. A single additional test board for each experimental leg was assembled to provide samples for time zero, baseline solder joint analysis.

Stencil Design and Printed Solder Paste Volume

The stencil aperture designs for the component lands on the PCB are shown in Figure 4. The aperture design was established to meet the requirement of the solder-paste volume-to-BGA ball volume (PBV) ratio between 0.5 and 0.6. This is the PBV ratio range which generates the maximum temperature cycling reliability of the BGA solder joints [6]. The area ratios for the stencil apertures for the CABGA192 and CTBGA84 are 1.31 and 0.69, respectively, and both are above the 0.6 minimum IPC standard. A laser cut stencil was used with a nominal stencil thickness for all legs of 101.6 µm (4 mils).

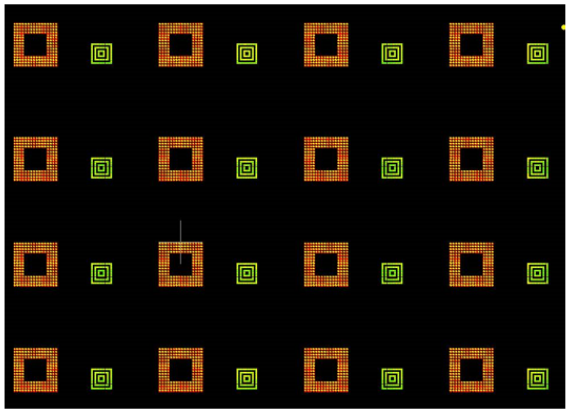

Package	Description above	Dimension		Geometry	Paste-to-Ball Volume Ratio
CABGA192		0.53 mm	21 mils	Square	0.57
CTBGA84		0.28 mm	11 mils	Square	0.56

Figure 4: Stencil aperture designs for the two components on the Alloy ATC TV board [37].

A Galaxy ASM DEK stencil printer was employed to print the solder pastes on the boards. The solder paste volume printed on each land of the Alloy ATC TV board was measured using a Koh Young Aspire KY6070XL Solder Paste Inspection (SPI) tool.

Figure A-1 in Appendix A plots the variability chart for the printed solder paste volume for each of the boards for which the fatigue data is reported in this study. Most points measured fell within the 50% and 150% lower and upper control limits respectively. Of the 10 points that fell outside the control limits, 7 were on the low end, and 6 were from the JRP (resin) solder paste type legs.

The plot in Figure A-1 indicates that the means of the paste transfer efficiency for the CTBGA84 component are lower than for the CABGA192 component for most solder pastes. This is expected since the area ratio for the former component is lower. A variance component analysis for the main effects, estimated that the 17.3% of the variation occurred across the two types of component land patterns, 17.6% variation occurred from board to board, only 5.6% occurred across solder pastes (code name), but the largest variation (57.9%) was within a board. No variation could be attributed across the solder paste types.

Reflow Soldering Profiles

The Appendix A contains the reflow profiles for all 7 experimental legs in Figures A-2, A-3, A-4, A-5, A-6, A-7 and A-8. These reflow profiles were measured using the KIC thermal profiler. The thermocouple locations on the Alloy ATC TV board are shown in Figure A-7 in Appendix A.

Two critical parameters in a reflow profile are the Peak Reflow Temperature (PRT) and the Time Above Liquidus (TAL). These are critical to ensure a good quality BGA solder joint, both for a homogeneous microstructure, to enable complete collapse, and a hybrid (heterogeneous) macrostructure to enable adequate mixing of the molten solder paste with the unmelted BGA solder ball.

The typical metric to measure reflow time is Time Above Liquidus (TAL), which is the temperature at which the entire solder paste is molten. The metallurgical compositions of the solders used in this study are near-eutectic or hypo-eutectic. So, the temperature at which the "Initial Melting" or onset of melting, which is usually the eutectic temperature of the metallurgical system of the solder in the paste, and the Liquidus, which is the temperature when the solder paste is fully molten will be different; even significantly different in one case, as seen in Table 3 that listed these two values for the five solder pastes evaluated in this study.

Table 3. Wt.% Bi, Wt.% Ag, Initial Melting and Liquidus Temperatures of the five solder pastes used in this study [37].

Code Name	Raja Kunyit	Red Flesh	Sultan 2	Beserah	Golden Pillow 2
Solder Paste Type	SAC	Ductile BiSn		JRP (Resin)	
Wt.% Bi	0	40	56-58	58	58
Wt.% Ag	3	0	<1	0	0
Initial Melting Temp, °C	217	139	138	139	140
Liquidus Temp, °C	220	179	145	139	140

The PRT and TAL values for the 5 legs are plotted together in Figure 5. As expected, the LTS legs are all lower in Peak Reflow Temperature (PRT) as compared to the Raja Kunyit (SAC305) leg. The JRP (Resin) legs are even lower than the

Ductile BiSn legs. The Beserah paste has an extended TAL to ensure the resin is sufficiently cured after reflow soldering. The Red Flesh Ductile BiSn leg has the shortest TAL. This is because it has the largest difference between the initial melting temperature and the liquidus temperature. The TAL is significantly more for the Sultan 2 solder paste than the Red Flesh solder paste. However, the post reflow microstructure of the Hybrid (SAC-BiSn) solder joints is influenced predominantly by the PRT and less so by the TAL. The higher PRT results in a more refined grain structure post reflow [40].

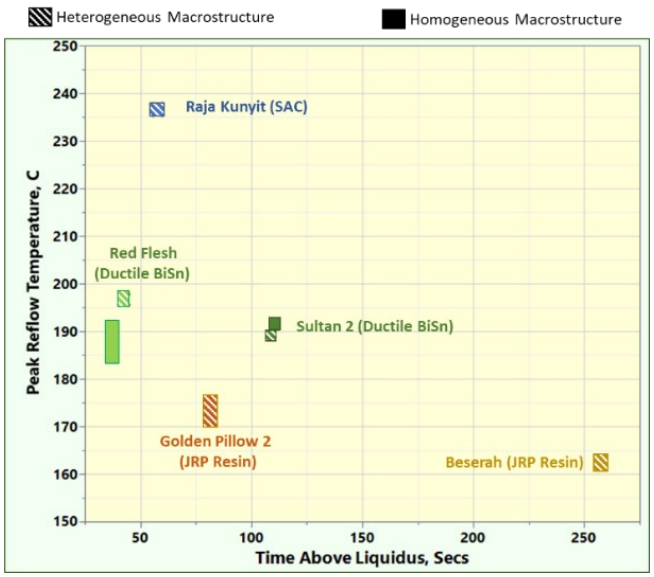

Figure 5. The Peak Reflow Temperature (C), and Time Above Liquidus (seconds) for the alloys used in this study [37].

Post Reflow Soldering Daisy Chain Resistances

The daisy chain resistances were measured for all 16 components of each type on each board after the boards were reflow soldered. Figure A-10 in Appendix A shows the daisy chain resistance plot. Some daisy chain resistance values for the CTBGA84 in the Golden Pillow 2 leg are outliers (see red square data points in Figure A-10). Figure 6 shows 3D Computer Tomography (CT) X-ray images and scanning electron microscopy images in the backscattered electron (BSE) mode of joints with the appearance of a Head-on-Pillow (HoP) solder defect.

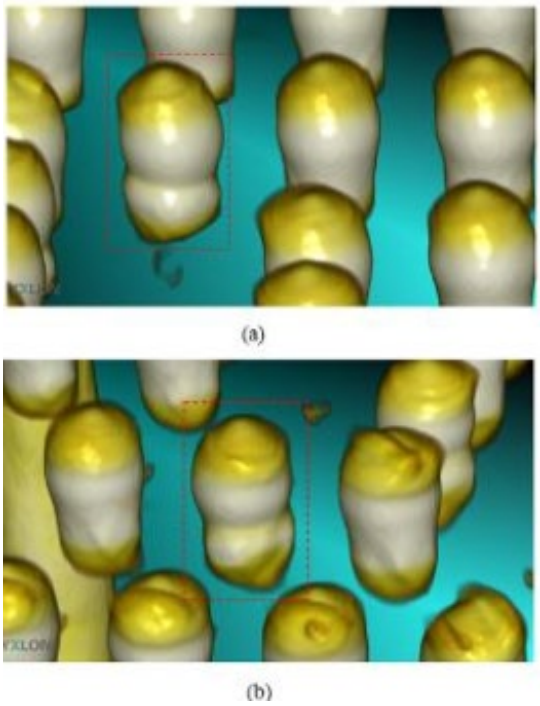

Figure 6. Examples of HoP-like solder joints in the Golden Pillow 2 JRP leg of CTBGA84 components (figures published previously [37]).

Similar solder joint structures were reported in the Process development phase of the current iNEMI LTSPR project [22]. These defects are believed to form by the premature gelling of the resin in the JRP paste before the solder has become molten and has wet the BGA SAC sphere. Increasing the initial ramp rate of the reflow profile for this Golden Pillow 2 leg is one suggested method to eliminate these defects.

Microstructural Characterization and Failure Analysis

Baseline characterizations were performed on representative board level assemblies from each of the test cells to document the solder joint quality and basic solder microstructure at time zero, before the start of temperature cycling. This enabled comparisons to be made between samples at time zero to samples that were removed subsequently from the temperature cycling chamber for characterization and failure mode analysis.

Microstructural characterizations and failure mode analyses were done using metallographic cross-sectioning and the Scanning Electron Microscope (SEM) operating in the Backscattered Electron (BSE) imaging mode. With BSE imaging, the number of electrons reaching the detector is proportional to the atomic number (Z), which makes it effective for differentiating phases. This has been demonstrated for SAC microstructures [41-43] and is

particularly useful for differentiating the high-*Z* Bi phase in solder microstructures [26, 41, 43]. The SEM operating in the secondary electron imaging (SEI) mode was used to observe the resin fillets.

Accelerated Temperature Cycling

Accelerated temperature cycling (ATC), or thermal cycling (TC), is the recognized technique for evaluating the thermal fatigue performance of solder attachments. Daisy chained components and circuit boards enable electrical continuity testing after surface mount assembly and in situ, continuous monitoring during thermal cycling. The thermal cycling plan includes two distinct thermal cycling profiles, 0/100 °C and -15/85 °C. The 0/100 °C profile is designated as TC1 in the IPC-9701B performance document that provides guidance for assessing reliability of surface mount attachments [44]. This test profile has nominal hot and cold ramp and dwell times of 10 minutes each (40-minute total cycle time).

The -15/85 °C profile is not part of the IPC-9701B standard, but there was a particular reason for using this thermal cycling profile, a reason directly related to the lower melting temperature of the Bi-Sn solder.

The homologous temperature, T_h is defined as the ratio of the temperature a material is at, T, and its melting point, T_m, with the calculation done on the Kelvin scale; $T_h = T(K)/T_m(K)$. Material degradation processes, such as creep that occurs when subjected to fatigue stresses, as well as annealing processes, such as recrystallization and grain growth of the microstructure within metals, occur at T_h greater than 0.4 [45]. At temperatures where T_h is greater than 0.9, the strength and hardness of metals reduces precipitously. This thermal cycling profile was used mainly due to the concern that the upper dwell temperature of 100 °C in the original temperature cycling profile (0/100 °C) was above a homologous temperature of 0.9 for BiSn solders.

Figure 7 displays the homologous temperature comparison between Sn-Ag-Cu solder and Bi-Sn solder. Since Bi-Sn solder has a lower melting point (~138 °C) than Sn-Ag-Cu solder (~217 °C), its homologous temperature line is above that of Sn-Ag-Cu. At the upper dwell temperature of 100 °C for the 0/100 °C thermal cycling test, T_h for Bi-Sn solder is 0.92. To lower the T_h below 0.90, 85 °C was chosen as the upper dwell temperature for an alternate thermal cycling profile. The T_h for Bi-Sn solder at 85 °C is 0.87. The T_h for SAC is 0.73 at 85 °C.

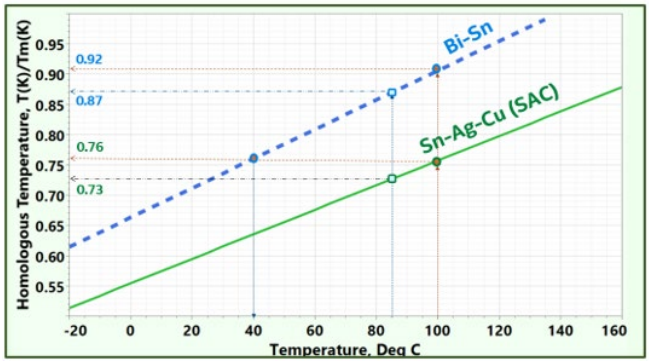

Figure 7: Homologous Temperature (T_h) Comparison between Sn-Ag-Cu solder and Bi-Sn solder [45].

The difference between the two thermal cycling dwell temperature extremes (ΔT) is a critical parameter when selecting thermal cycling test profile since in the literature, many acceleration models that have been widely used to predict the lifetimes of solder joints of electronic packages include ΔT as a key factor [46-49]. Hence, the same 100 °C ΔT was set for the second thermal cycling profile to match the original 0/100 °C profile. Consequently, the dwell temperature extremes for this second profile were set at -15 °C to 85 °C.

Nonetheless, since the paramount goal in this work was to compare the temperature cycling fatigue resistance of SAC and Bi-Sn BGA solder joints, setting the upper dwell temperature of the second thermal cycling profile at the same T_h of that for SAC at 100 °C would have been most appropriate. However, from Figure 7 it is apparent that this would require the upper dwell temperature to be at 40 °C. Using a -40 to 40 °C temperature profile would be impractical since the time needed to get adequate solder joint failures would extend beyond 3 to 5 years.

During thermal cycling, the solder joints are monitored using an event detector set at a resistance limit of ≥1000 ohms. Failure data are reported as characteristic life η (the number of cycles to achieve 63.2% failure), Weibull slope β, Correlation Coefficient r^2, and 1% Cumulative Failure from a two-parameter (2-P) Weibull analysis.

RESULTS AND DISCUSSION

Solder Joint Characterization

During the reflow assembly process, the SnBi-based solder paste melts and wets the SAC balls and Cu metallization on the PCB pads. Sn and Cu dissolve into the melt until it reaches equilibrium. The microstructure and Bi distribution of hybrid joints after SMT reflow depend on variables such as reflow peak temperature, initial solder paste to solder ball volume ratio, cooling rate, and solder composition [55, 56]. Figure 8 shows low magnification BSE and SEI images of as assembled CABGA192 samples. JRP assemblies are shown in Figure 8a through Figure 8d, and hybrid assemblies are shown in Figure 8e and Figure 8f [37]. As discussed in the assembly section, the stencil aperture was designed to produce an initial solder-paste volume-to-BGA ball volume (PBV) ratio of between 0.5 and 0.6 for all four hybrid assemblies.

Despite a constant volume ratio, there is a noticeable variation in the amount of Bi mixing in the solder joints imaged in Figure 8. This variation in Bi mixing could result from different peak reflow temperatures and time above liquidus (Figure 5), different flux chemistries, as well as compositional differences in Bi content and minor alloy additions of the pastes.

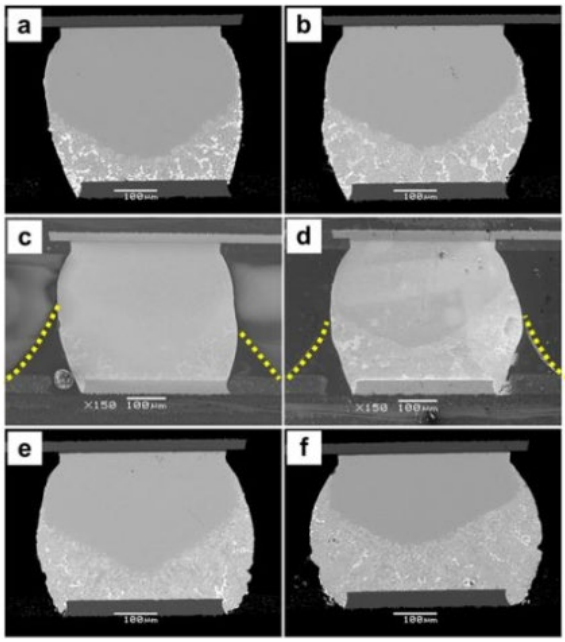

Figure 8. Cross sectional images of hybrid and JRP CABGA192 LTS solder joints before thermal cycling. Bismuth mixing is revealed using BSE imaging in a) Beserah JRP and b) Golden Pillow 2 JRP. Resin fillet formation is outlined in SEI images in c) Beserah JRP and d) Golden Pillow 2 JRP. Bismuth mixing is revealed using BSE imaging in e) hybrid Red Flesh and f) hybrid Sultan 2 (figures published previously [37]).

The amount of Bi mixing was estimated using ImageJ, a public domain Java image processing program available from the National Institute of Health (NIH)) [52]. Sixteen solder joints for each leg were imaged using the SEM and the back scattered detector. The area of Bi mixed region was measured with respect to the area of entire joint. Figure 9 shows the average values of Bi mixing for four experimental legs. For the CABGA192 hybrid solder joints, Beserah JRP has the lowest average Bi mixing and Sultan 2 has the highest average Bi mixing.

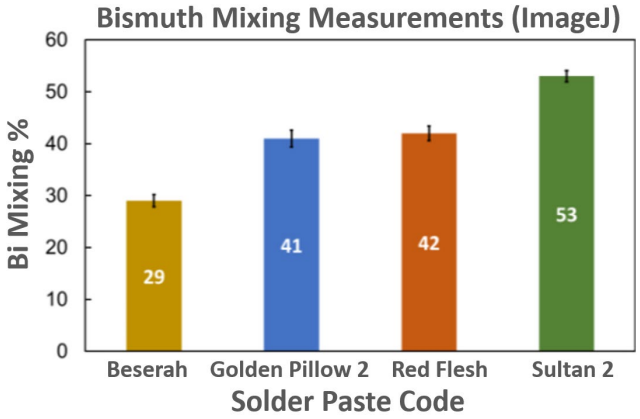

Figure 9. A plot of average solder joint Bi mixing levels in the CABGA192 hybrid and JRP legs estimated using ImageJ processing [37].

Figure 10 shows the solder joint microstructures of as assembled CABGA192 homogeneous Red Flesh and homogeneous Sultan 2 samples [37]. In general, the distributions of the Bi phase in both homogeneous assemblies are similar. There are two distinct Bi precipitate morphologies, with large primary Bi particles and small plate-like precipitates. Sultan 2 has more prominent large primary Bi precipitates and finer, close spaced plate-like precipitates. These findings are consistent with the work of Belyakov et al. who identified two types of Bi phases in Bi containing solders. They described the two Bi morphologies as large, chunky Bi particles that form in the grain boundary during solidification and as small Bi plates that precipitate in the solid state [53].

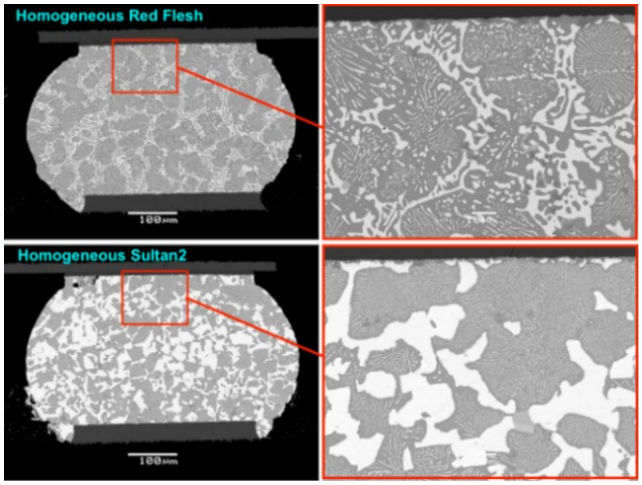

Figure 10. Cross sectional solder joint images of sample CABGA192 components with a) homogeneous Red Flesh and b) homogeneous Sultan 2 before thermal cycling. Results published previously [37].

Accelerated Temperature Cycling Results

This section includes the CABGA192 Accelerated Temperature Cycling (ATC) Weibull statistics, distribution plots and a summary analysis of this data.

- Figure 11 is a bar chart comparing the characteristic lifetimes of the CABGA192 component for all LTS alloy test legs from the 0/100 °C and -15/85 °C thermal cycling profiles.
- Figure 12 is a bar chart comparing the 1% cumulative failure values of the CABGA192 component for all LTS alloy test legs from the 0/100 °C and -15/85 °C thermal cycling profiles.
- Figure 13 and Figure 14 are bar charts including the CABGA192 component 1% cumulative failure and characteristic lifetime statistics from the 0/100 °C and -15/85 °C thermal cycling profiles respectively. The Weibull statistics for both thermal cycling profiles are summarized in Table 4.
- Figure 15 is a composite Weibull distribution plot for all 7 test legs, from the 0/100 °C and -15/85 °C thermal cycling profiles respectively.

Additional Weibull distribution plots show specific performance comparisons:

- Figure 16: Hybrid Red Flesh, Hybrid Sultan 2 and SAC305 baseline
- Figure 17: Homogeneous Red Flesh, Homogeneous Sultan 2 and SAC305 baseline
- Figure 18: Beserah JRP, Golden Pillow 2 JRP, and SAC305 baseline

Figures 16, Figure 17, and Figure 18 are also presented in Appendix B with 90% confidence intervals overlaid.

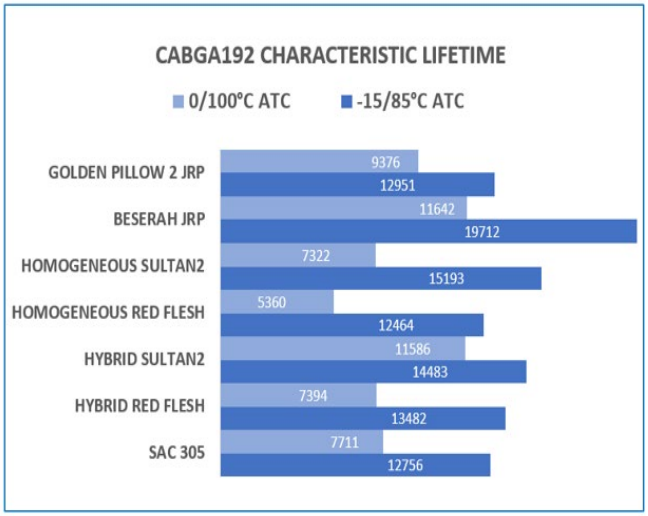

Figure 11. A bar chart comparing the characteristic lifetimes of the CABGA192 component for all LTS alloy test legs from the 0/100 °C (results published previously [37]) and -15/85 °C ATC profiles.

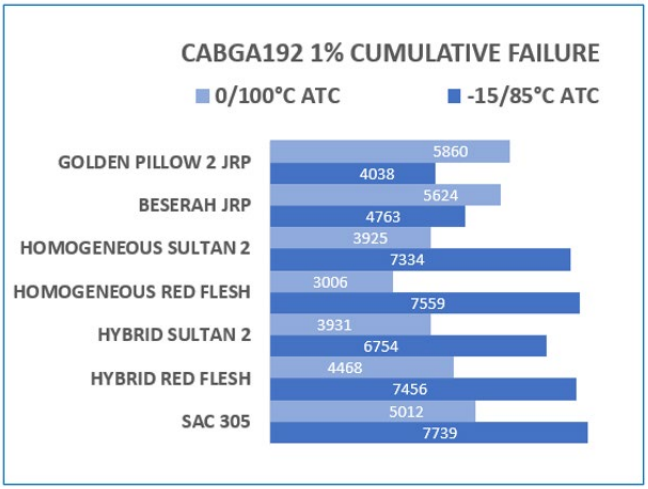

Figure 12. A bar chart comparing the 1% cumulative failure values of the CABGA192 component for all LTS alloy test legs from the 0/100 °C (results published previously [37]) and -15/85 °C ATC profiles.

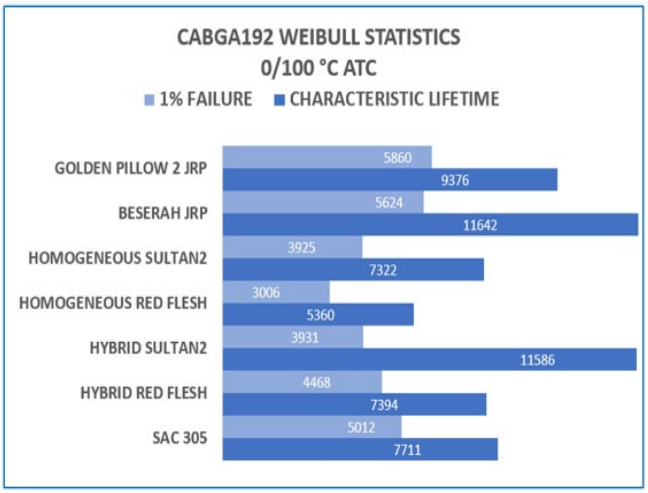

Figure 13. CABGA192 component 1% cumulative failure and characteristic lifetime statistics from the 0/100 °C ATC profile (results published previously [37]).

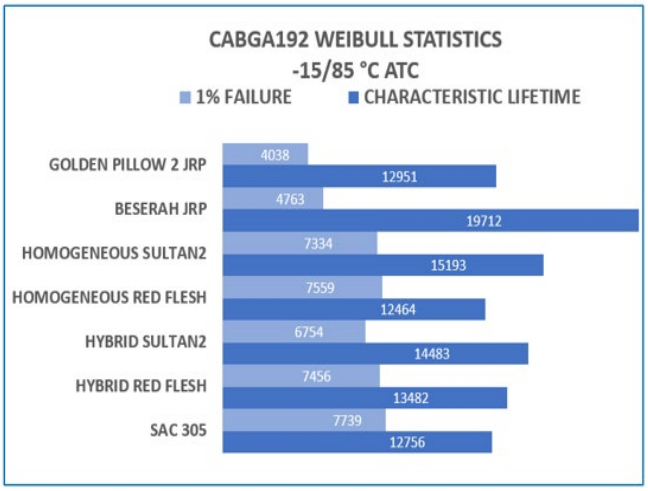

Figure 14. CABGA192 component 1% cumulative failure and characteristic lifetime statistics from the -15/85 °C ATC profile.

CABGA192 Weibull Statistics for 0/100 °C Thermal Cycling				
Solder Assembly Type	Characteristic Lifetime η (cycles)	1% Failures (cycles)	Slope β	Correlation Coefficient, r^2
SAC Baseline	**7711**	**5012**	**10.7**	**0.97**
Hybrid Red Flesh	7394	4468	9.1	0.94
Hybrid Sultan 2	11586	3931	4.3	0.96
Homogeneous Red Flesh	5360	3006	5.3	0.96
Homogeneous Sultan 2	7322	3925	7.4	0.92
Beserah Joint Reinforced Paste	11642	5624	7.4	0.92
Golden Pillow 2 Joint Reinforced Paste	9376	5860	9.8	0.92

CABGA192 Weibull Statistics for -15/85 °C Thermal Cycling				
Solder Assembly Type	Characteristic Lifetime η (cycles)	1% Failures (cycles)	Slope β	Correlation Coefficient, r^2
SAC Baseline	**12756**	**7739**	**9.2**	**0.99**
Hybrid Red Flesh	13482	7456	7.8	0.97
Hybrid Sultan 2	14483	6754	6.0	0.98
Homogeneous Red Flesh	12464	7559	9.2	0.97
Homogeneous Sultan 2	15193	7334	6.3	0.97
Beserah Joint Reinforced Paste	19712	4763	3.2	0.98
Golden Pillow 2 Joint Reinforced Paste	12951	4038	3.9	0.99

Table 4. Summary of Weibull statistics for the CABGA192 component 0/100 °C ATC profile (results published previously [37]) and the CABGA192 component -15/85C °C ATC profile.

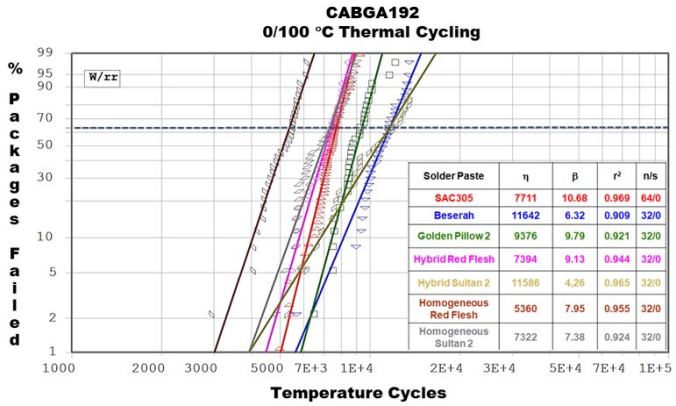

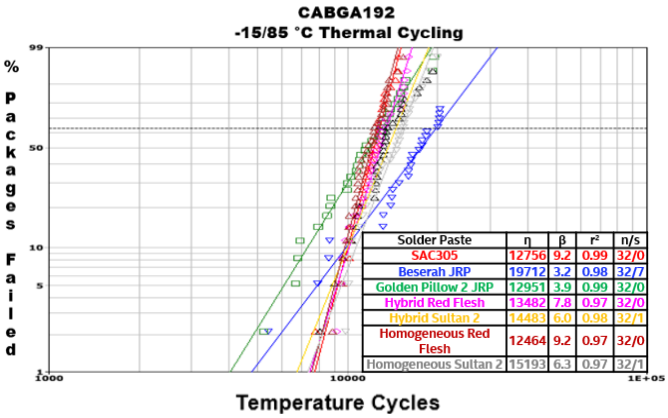

Figure 15. CABGA192 composite Weibull distribution plots showing thermal cycling results for 6 LTS legs and the SAC305 baseline from the 0/100 °C ATC profile (results published previously [37]) and the -15/85 °C ATC profile.

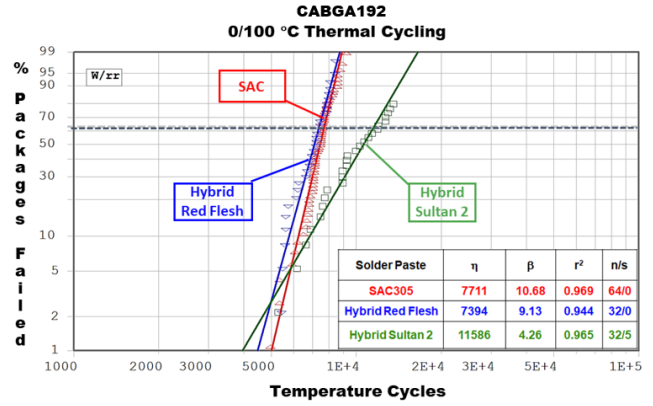

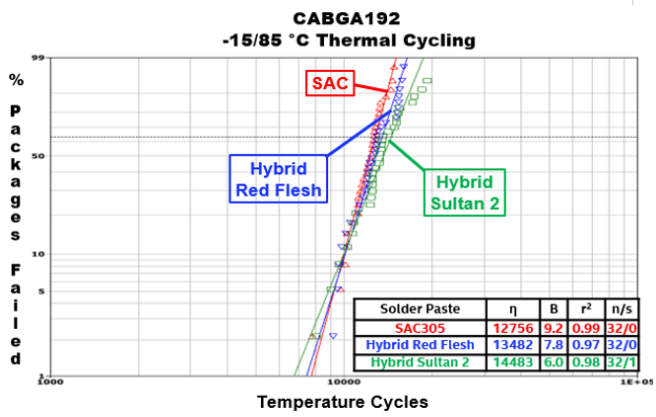

Figure 16. CABGA192 Weibull distribution plots showing thermal cycling results for Hybrid Red Flesh, Hybrid Sultan 2 and SAC305 baseline from the 0/100 °C ATC profile (results published previously [37]) and the -15/85 °C ATC profile.

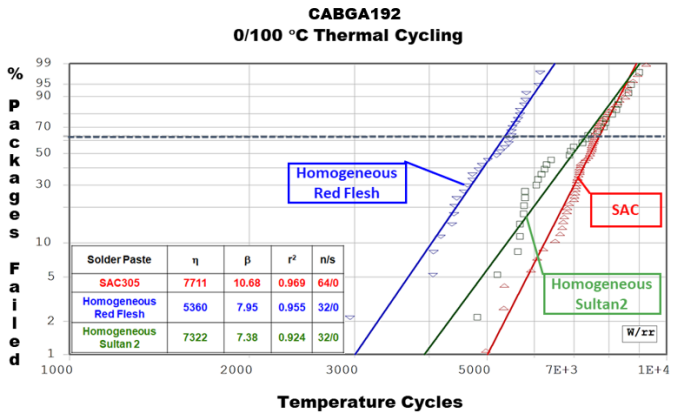

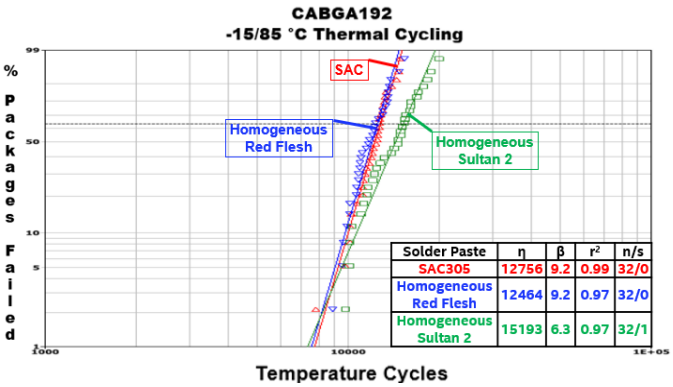

Figure 17. CABGA192 Weibull distribution plots showing thermal cycling results for Homogeneous Red Flesh, Homogeneous Sultan 2 and SAC305 baseline from the 0/100 °C ATC profile (results published previously [37]) and the -15/85 °C ATC profile.

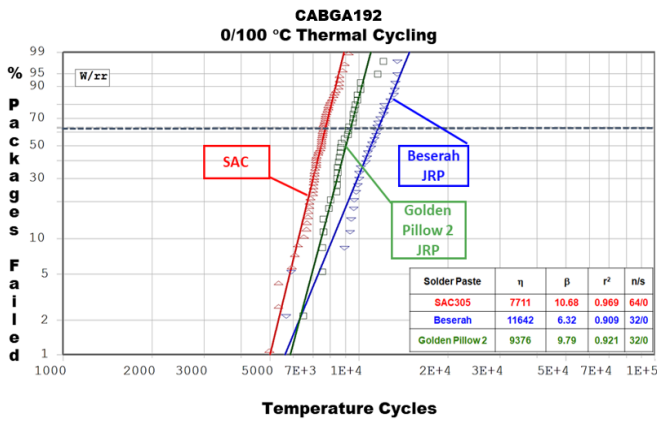

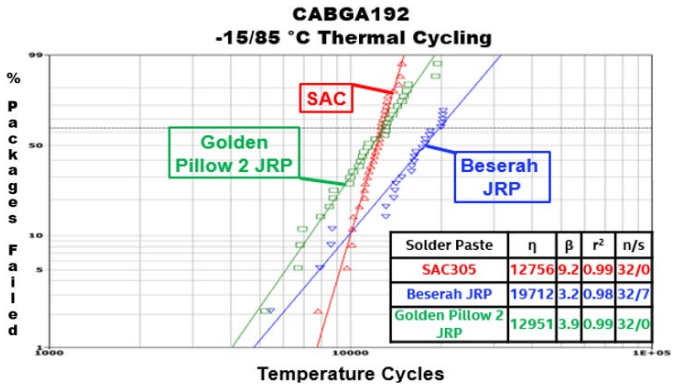

Figure 18. CABGA192 Weibull distribution plots showing thermal cycling results for Beserah JRP, Golden Pillow 2 JRP and SAC305 baseline from the 0/100 °C ATC profile (results published previously [37]) and the -15/85 °C ATC profile.

The Weibull plots in Figure 15, along with the Table 4 summary, show the CABGA192 component Weibull characteristic lifetime and 1% cumulative failure data for all test legs in the 0/100 °C and -15/85 °C ATC profiles. From a characteristic lifetime analysis, we see that all test legs, except for the homogeneous Red Flesh from the 0/100 °C profile which shows a relatively lower performance (which was not the case for this component as run in the -15/85 °C profile), have a thermal cycling performance comparable to, or increased from, the SAC305 performance baseline. A key observation is that the relatively lower component characteristic lifetime performance for homogeneous Red Flesh in the 0/100 °C profile went away when this part was run in the less aggressive -15/85 °C profile.

From a 1% cumulative failure analysis, we see that both homogeneous Red Flesh and homogeneous Sultan 2 show relatively lower performance (even with the 90% Confidence Intervals overlaid in Appendix B) as compared with the SAC305 baseline in the 0/100 °C profile. Additionally, we see that both the Beserah JRP and Golden Pillow 2 JRP show relatively lower 1% cumulative failure performance (even

with the 90% Confidence Intervals overlaid in Appendix B), as compared to the SAC305 baseline in the -15/85 °C profile. A key observation is that the relatively lower 1% cumulative failure performance from the homogeneous Red Flesh and homogeneous Sultan 2 legs in the 0/100 °C profile went away when this part was run in the less aggressive -15/85 °C profile.

Figure 16 and its companion plot with 90% Confidence intervals in Appendix B show that hybrid Red Flesh and hybrid Sultan 2 have nearly identical or increased characteristic lifetime performance for the CABGA192 component, across the 0/100 °C and -15/85 °C profiles, as compared with the SAC305 baseline. The Weibull slope β for hybrid Sultan 2 is noticeably lower than SAC305 across the 0/100 °C and -15/85 °C profiles, extrapolating to a substantially larger characteristic lifetime for hybrid Sultan 2 but a lower 1% cumulative failure (Table 4), but the difference is minimal when 90% Confidence Internals are overlaid (as shown in Appendix B).

Figure 17 and its companion plot with 90% Confidence intervals in Appendix B show that homogeneous Sultan 2, across the 0/100 °C and -15/85 °C profiles, and homogeneous Red Flesh, in the -15/85 °C profile, have comparable or increased characteristic lifetime performance for the CABGA192 component as compared with the SAC305 baseline. The homogeneous Red Flesh shows relatively lower characteristic lifetime and 1% cumulative failure performance, in the 0/100 °C profile, as compared with the SAC305 baseline, but this difference went away in the less aggressive -15/85C profile. The homogeneous Sultan 2 shows relatively lower 1% cumulative failure performance (even with the 90% Confidence Intervals overlaid in Appendix B), in the 0/100 °C profile, as compared with the SAC305 baseline, but this difference also went away in the less aggressive -15/85C profile.

Figure 18 and its companion plot with 90% Confidence intervals in Appendix B show that Beserah JRP and Golden Pillow 2 JRP have similar or increased characteristic lifetime performance for the CABGA192 component, across the 0/100 °C and -15/85 °C profiles, as compared with the SAC305 baseline. The Beserah JRP and Golden Pillow 2 JRP show relatively lower 1% cumulative failure performance (even with the 90% Confidence Intervals overlaid in Appendix B), in the -15/85 °C profile, as compared to both the 0/100 °C profile and to the SAC305 baseline.

Table 5 shows the CABGA192 component characteristic lifetime ratio comparisons, to see the direct impact of these two thermal cycle profiles on characteristic lifetimes. This ratio is calculated by dividing the characteristic lifetime of the -15/85 °C thermal cycling profile by the characteristic lifetime of the 0/100 °C profile. Data analysis shows the characteristic lifetime of the SAC baseline with the less aggressive -15/85 °C profile was extended by a factor of 1.65X compared to the 0/100 °C profile. The Beserah JRP ratio of 1.69X was comparable to the SAC baseline, while the Hybrid Red Flesh ratio of 1.82X, the Sultan 2 ratio of 2.07X, and the Homogeneous Red Flesh ratio of 2.33X were all extended beyond the SAC baseline in the less aggressive -15/85 °C profile. However, the Hybrid Sultan 2 ratio of 1.25X and the Golden Pillow 2 JRP ratio of 1.38X both show a decrease in the ratio versus the SAC baseline in the less aggressive -15/85 °C profile.

CABGA192 WEIBULL STATISTICS ; CHARACTERISTIC LIFETIME THERMAL CYCLE PROFILE RATIO COMPARISON			
LEG NAME	0/100°C ATC PROFILE	-15/85°C ATC PROFILE	RATIO = -15/85 °C / 0/100 °C
SAC Baseline	**7711**	**12756**	**1.65X**
Hybrid Red Flesh	7394	13482	1.82X
Hybrid Sultan 2	11586	14483	1.25X
Homogeneous Red Flesh	5360	12464	2.33X
Homogeneous Sultan 2	7322	15193	2.07X
Beserah JRP	11642	19712	1.69X
Golden Pillow 2 JRP	9376	12951	1.38X

Table 5. CABGA192 component characteristic lifetime ratio comparison of the 0/100 °C ATC profile (results published previously [37]) and -15/85 °C ATC profile.

Table 6 shows the CABGA192 component 1% cumulative failure ratio comparisons, to see the direct impact of these two thermal cycle profiles on 1% cumulative failure. This ratio is calculated by dividing the 1% cumulative failure of the -15/85 °C thermal cycling profile by the 1% cumulative failure of the 0/100 °C profile. The 1% cumulative failure of the SAC baseline with the less aggressive -15/85 °C profile was extended by a factor of 1.54X compared to the 0/100 °C profile. The Hybrid Red Flesh ratio of 1.67X, the Hybrid Sultan 2 ratio of 1.72X, the Homogeneous Sultan 2 ratio of 1.87X and the Homogeneous Red Flesh ratio of 2.51X were all extended beyond the SAC baseline in the less aggressive -15/85 °C profile. However, the Beserah JRP ratio of 0.85X and the Golden Pillow 2 JRP ratio of 0.69X both show a relatively large decrease in the ratio versus the SAC baseline in the less aggressive -15/85 °C profile.

CABGA192 WEIBULL STATISTICS ; 1% CUMULATIVE FAILURE THERMAL CYCLE PROFILE RATIO COMPARISON			
LEG NAME	0/100°C ATC PROFILE	-15/85°C ATC PROFILE	RATIO = -15/85 °C / 0/100 °C
SAC Baseline	**5012**	**7739**	**1.54X**
Hybrid Red Flesh	4468	7456	1.67X
Hybrid Sultan 2	3931	6754	1.72X
Homogeneous Red Flesh	3006	7559	2.51X
Homogeneous Sultan 2	3925	7334	1.87X
Beserah JRP	5624	4763	0.85X
Golden Pillow 2 JRP	5860	4038	0.69X

Table 6. CABGA192 component 1% cumulative failure ratio comparison of the 0/100 °C ATC profile (results published previously [37]) and -15/85 °C ATC profile.

Failure Mode Analysis: Thermal Fatigue

The microstructural response of SAC solder joints during thermal cycling is well known. The coarsening of the network of Ag_3Sn precipitates is followed by recrystallization and propagation of cracks along the newly formed Sn boundaries. BGA thermal fatigue failures in Sn-based solders typically have a crack path through the strain-localized region of the bulk solder, although propagation may proceed close to the IMC interfacial layer. The fracture path is characterized by local recrystallization, global recrystallization, crack branching, and cavitation at boundary triple points (for example, at the triple junction between the solder, land and solder mask). These are common fracture characteristics for SAC solder thermal fatigue failures and are consistent with those reported first by Dunford in 2004 [54] and confirmed in many previous publications [37, 41, 42, 43, 55, 56].

Figure 19 and Figure 20 show Backscattered Scanning Electron Microscope (SEM) images of failed thermally cycled solder joints from CABGA192 SAC baseline samples, from the 0/100 °C profile (results published previously [37]) and the -15/85 °C profile respectively. Crack initiation and propagation is within the bulk solder close to the package side interface. Mostly partial cracking was observed near the PCB interface.

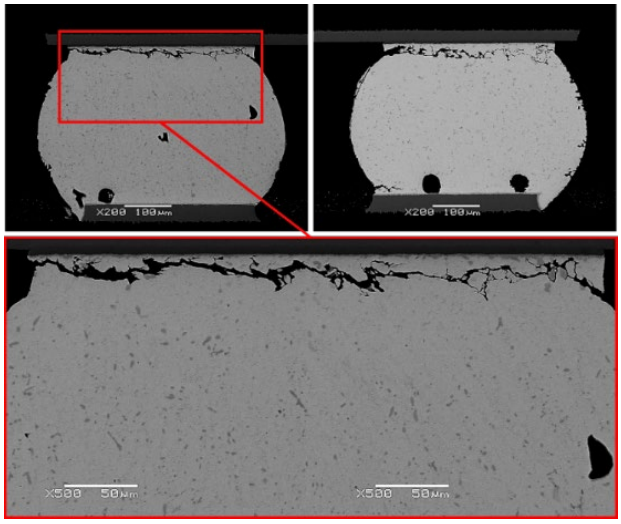

Figure 19. Backscattered SEM images of two failed thermal cycled solder joints from CABGA192 SAC baseline samples, 0/100 °C ATC profile (results published previously [37]).

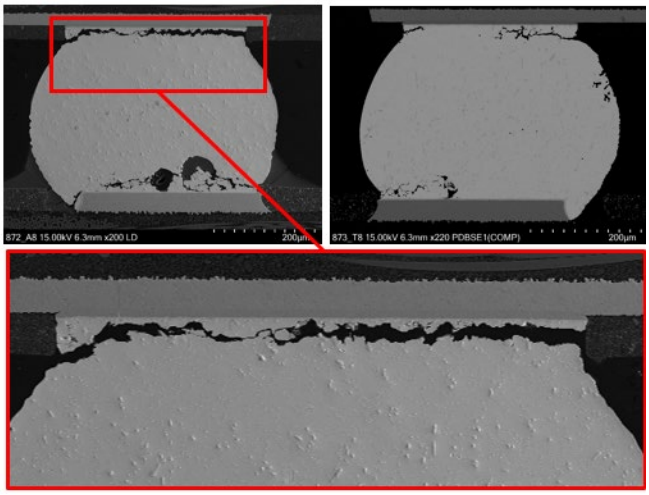

Figure 20. Backscattered SEM images of two failed thermal cycled solder joints from CABGA192 SAC baseline samples, -15/85 °C ATC profile.

Figures 21 through 32 show failed thermally cycled solder joints from the hybrid, homogeneous, and JRP CABGA192 samples from the 0/100 °C profile [37] and the -15/85 °C profile. In general, all test legs including hybrid Red Flesh (Figures 21 and 22), hybrid Sultan 2 (Figures 23 and 24), homogeneous Red Flesh (Figures 25 and 26), homogeneous Sultan 2 (Figures 27 and 28), Beserah JRP (Figures 29 and 30), and Golden Pillow 2 JRP (Figures 31 and 32) exhibit the same basic failure characteristics of the SAC305 baseline, with thermal fatigue cracking through the bulk solder near the package side. The backscattered SEM analysis found no evidence of Bi precipitation in the vicinity of package-side

cracking, even in hybrid Sultan 2, the hybrid assembly with the greatest Bi mixing level (Figure 9). However, when Bi is present in solid solution, it can affect thermal fatigue performance, and dissolved Bi cannot be detected with backscattered imaging. SEM-EDS (Energy Dispersive Spectroscopy) analysis could be performed to investigate the existence of dissolved Bi near the package interface.

The predominant fatigue failure location is at the package side in the unmelted SAC region. Less fatigue cracking was detected in the Bi-mixed region of some hybrid and JRP solder joints (Figures 21-22). Mostly partial cracking was observed in the Bi rich region near the PCB interface in some JRP and hybrid solder joints. This is consistent with Weibull plots for the hybrid and JRP assemblies that show no evidence of a bimodal distribution indicative of more than a single solder joint failure mechanism or crack propagation path. An example of a thermal fatigue failure in a Bi mixed region is shown in the lower image of Figure 21. The crack likely initiates at an incoherent boundary between Bi and Sn phases and propagates either along Sn grain boundaries, along a phase boundary between Bi precipitates and the Sn matrix, or through a large, coarsened Bi phase that has accumulated near the intermetallic (IMC) layer. This crack development process was also observed in both homogeneous Red Flesh and homogeneous Sultan 2 (Figures 25-28).

Figures 25-28 show voids in the failed CABGA192 homogeneous solder alloy assemblies. The voiding is located at adjoining large Bi precipitates or at Bi/Sn interfaces. Because minimal voiding was detected before thermal cycling (Figure 10), it is assumed that the voids were not initiated purely as a result of thermal cycling (but they could have grown in size). During thermal cycling, saturated Bi that is in solid solution in the Sn matrix transforms into a secondary Bi precipitate. It has been estimated that the precipitation of Bi causes about a 25% reduction in the localized volume [57]. This volume misfit generates an elastic strain energy that is proportional to the volume change during the phase transformation of precipitation. In turn, a tensile stress is introduced at the boundary between the Bi precipitate and the Sn matrix. This eventually causes separation between the phases resulting in the formation of a void [58]. This process is analogous to the cavitation voiding at boundary triple points in SAC solders that is responsible for tertiary creep during thermal cycling [54, 59].

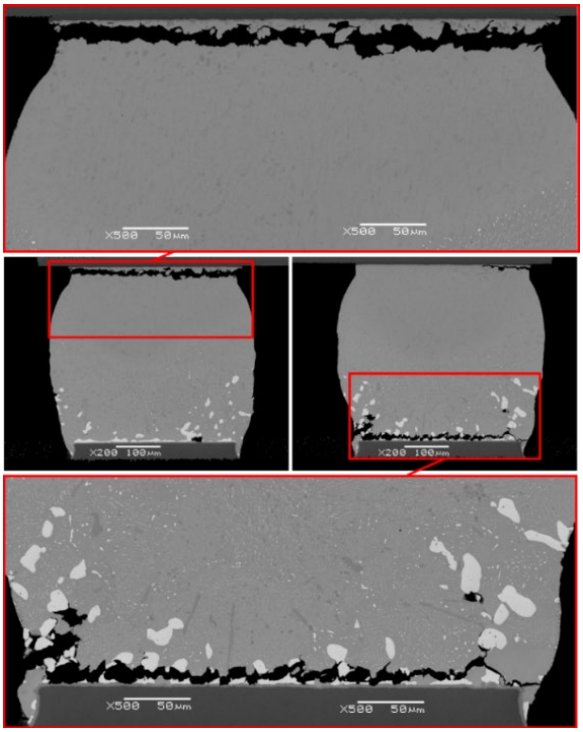

Figure 21. Backscattered SEM images of two failed thermal cycled solder joints from CABGA192 hybrid Red Flesh, 0/100 °C ATC profile (results published previously [37]).

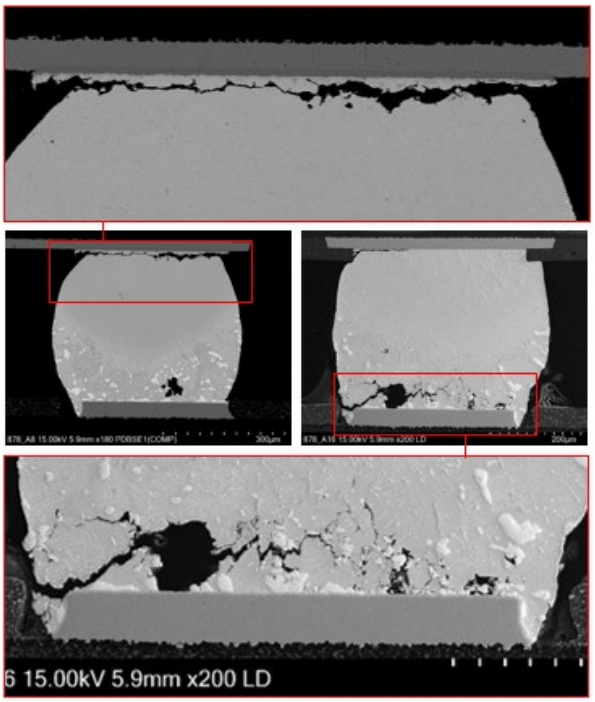

Figure 22. Backscattered SEM images of two failed thermal cycled solder joints from CABGA192 hybrid Red Flesh, -15/85 °C ATC profile.

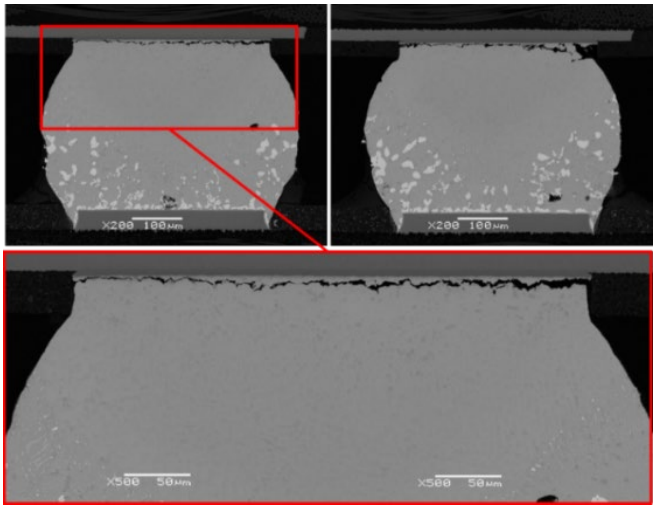

Figure 23. Backscattered SEM images of two failed thermal cycled solder joints from CABGA192 hybrid Sultan 2, 0/100 °C ATC profile (results published previously [37]).

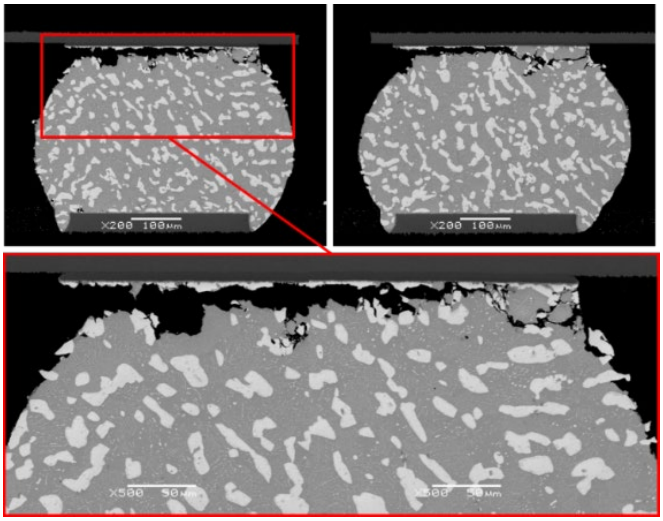

Figure 25. Backscattered SEM images of two failed thermal cycled solder joints from CABGA192 homogeneous Red Flesh, 0/100 °C ATC profile (results published previously [37]).

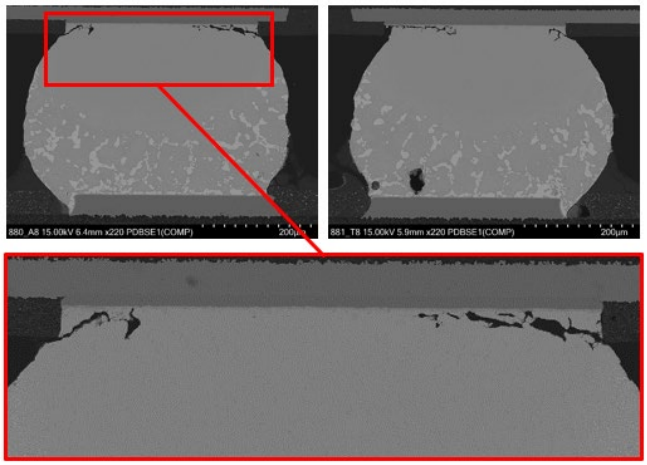

Figure 24. Backscattered SEM images of two failed thermal cycled solder joints from CABGA192 hybrid Sultan 2, -15/85 °C ATC profile.

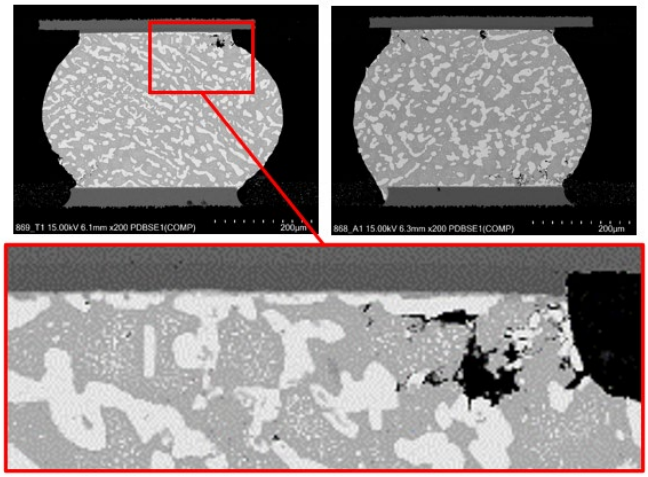

Figure 26. Backscattered SEM images of two failed thermal cycled solder joints from CABGA192 homogeneous Red Flesh, -15/85 °C ATC profile.

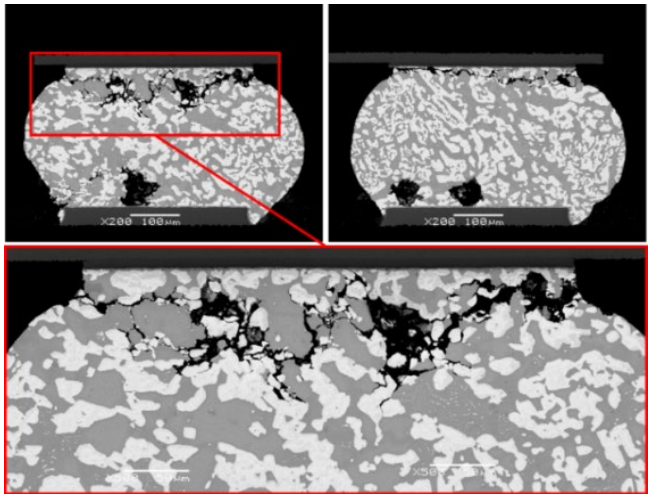

Figure 27. Backscattered SEM images of two failed thermal cycled solder joints from CABGA192 homogeneous Sultan 2, 0/100 °C ATC profile (results published previously [37]).

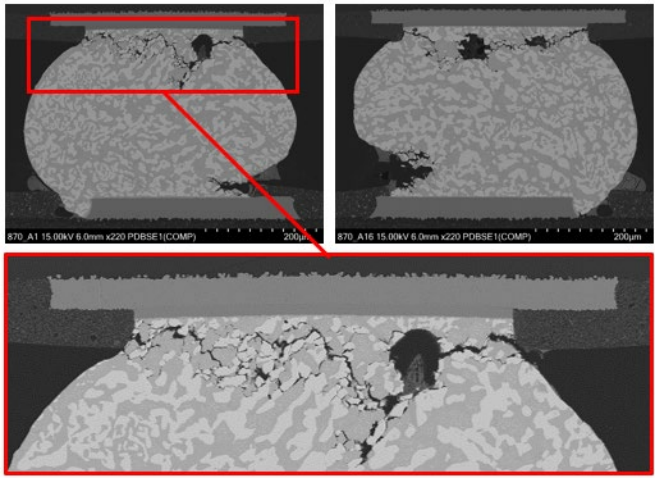

Figure 28. Backscattered SEM images of two failed thermal cycled solder joints from CABGA192 homogeneous Sultan 2, -15/85 °C ATC profile.

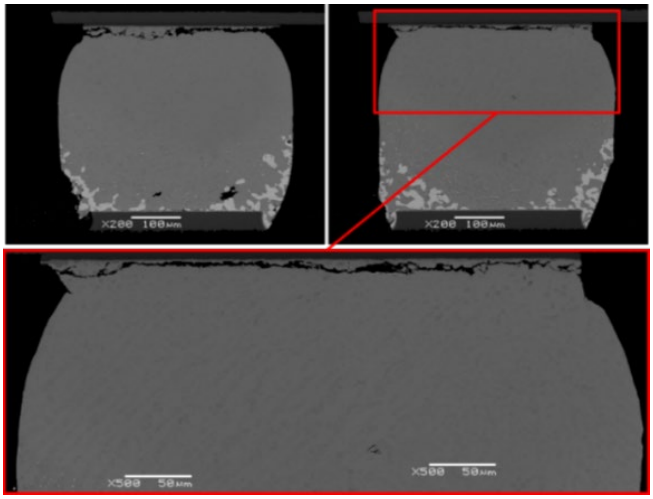

Figure 29. Backscattered SEM images of two failed thermal cycled solder joints from CABGA192 Beserah JRP, 0/100 °C ATC profile (results published previously [37]).

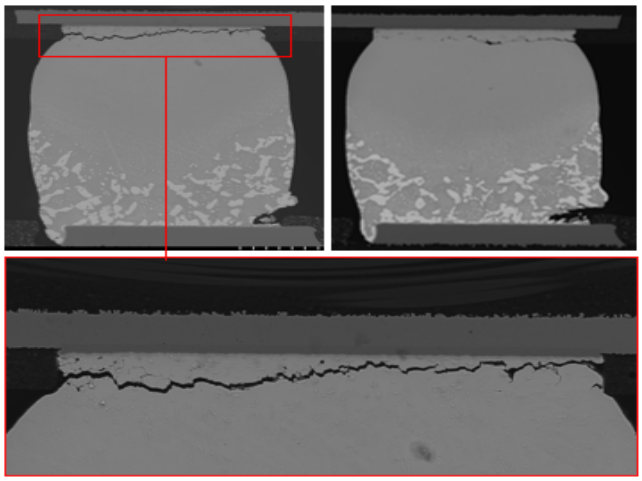

Figure 30. Backscattered SEM images of two failed thermal cycled solder joints from CABGA192 Beserah JRP, -15/85 °C ATC profile.

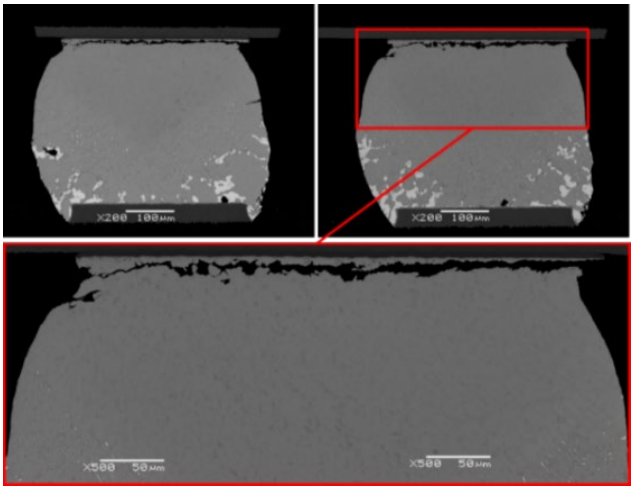

Figure 31. Backscattered SEM images of two failed thermal cycled solder joints from CABGA192 Golden Pillow 2 JRP, 0/100 °C ATC profile (results published previously [37]).

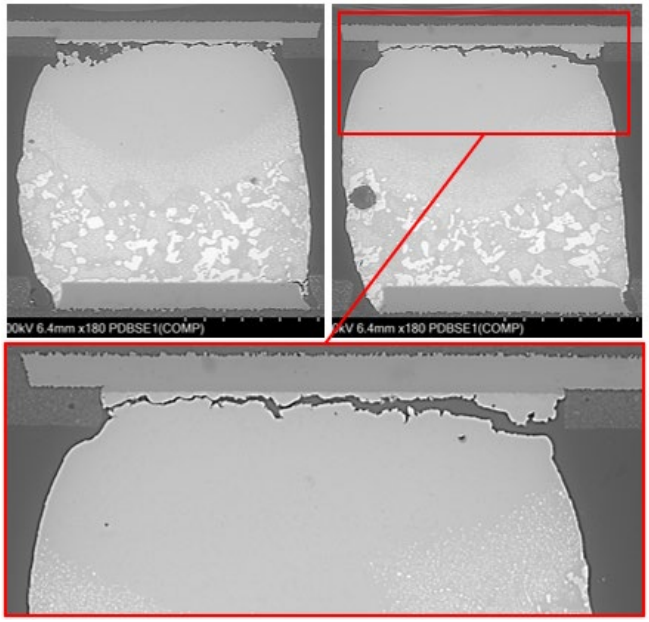

Figure 32. Backscattered SEM images of two failed thermal cycled solder joints from CABGA192 Golden Pillow 2 JRP, -15/85 °C ATC profile.

Observation of Solder Ball Drift

Solder ball drift is an interesting deformation phenomenon observed in thermally cycled hybrid LTS solder joints, first reported by Wentlent et al. in 2020 [60]. During X-ray inspection, it was noticed that in several locations the solder joints were noticeably shifted out of position. Those shifted positions were documented more clearly using destructive cross-sectional analysis.

Because of these findings, thermally cycled CABGA192 samples were inspected for solder ball drift using X-ray inspection and cross-sectional analysis. Previous work on the CABGA192 revealed multiple examples of solder ball drift in all experimental legs containing hybrid-type solder joints [37], and similar findings were revealed from inspection of the -15/85 °C profile. These solder ball drift examples include Beserah JRP, Golden Pillow 2 JRP, hybrid Red Flesh and hybrid Sultan 2. Solder ball drift was not found in hybrid assemblies prior to thermal cycling and was not found in homogeneous LTS or SAC assemblies. Dramatic examples of solder ball drift in thermally cycled CABGA192 samples are shown in the SEM cross sectional images in Figure 33.

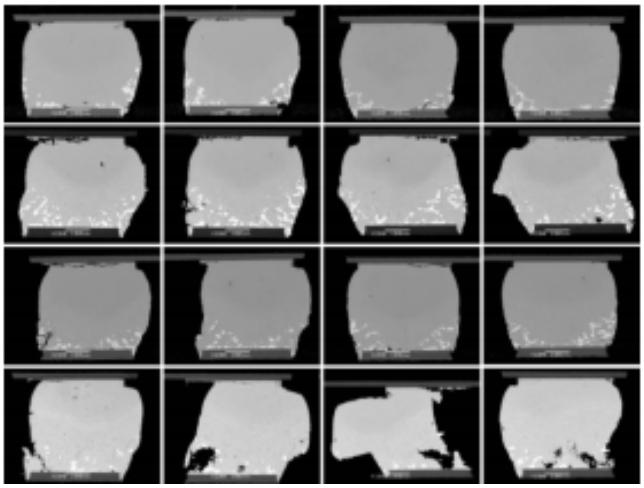

Figure 33. Multiple examples of ball drift in the CABGA192 component [results published previously [37]).

Figure 33 highlights an extremely interesting characteristic of solder ball drift. Severe solder ball drift is often found when there is no solder ball drift in adjacent solder joints that are expected to experience nearly the same strain induced by the CTE mismatch between the component and PCB. Solder ball drift also can be found at inner row locations and away from high-strain corner locations as shown in the top-down X-ray images of the CABGA192 (from the 0/100 °C profile [37] and the -15/85 °C profile) in Appendix C.

It is important to recognize that despite the severe deformation, drifted solder balls generally are not detached from the component interface and remain connected electrically. Thus, solder ball drift is not necessarily considered a primary failure mode, particularly one that would be detected by the resistance monitoring and event detection used in this study. Solder ball drift is an interesting phenomenon, but further detailed characterization is beyond the scope of this study.

SUMMARY

The thermal fatigue resistance of four Low Temperature Solder (LTS) alloys was assessed using a CABGA192 ball grid array test vehicle and accelerated thermal cycling profiles of 0 to 100 °C (IPC-9701B, TC1) and -15 to 85 °C. The original concern with the accelerated 0/100 °C thermal profile was that the Bi-Sn might not perform as well with the higher acceleration provided at an upper temperature extreme of 100 °C. As 100 °C is close to the onset of the low temperature solder melting temperature, it may result in a decrease in the strength of the solder, possibly lowering the characteristic lifetime. Additionally, most computer products, used by consumers, do not operate continuously at 100 °C. For both reasons, another profile with a lower upper temperature extreme was also used for this study. Thus the -15/85 °C accelerated profile was selected (after considering the homologous temperature comparison between Sn-Ag-Cu and Bi-Sn solder). Based on the results of this study, even with failures occurring faster with the 0/100 °C profile, the low temperature solders do perform well at 100 °C.

The alloys with code names Red Flesh and Sultan 2 were evaluated using a hybrid assembly process (SAC BGA with LTS solder paste) and a homogeneous assembly process (matching LTS BGA and LTS paste). The alloys with code names Beserah and Golden Pillow 2 were evaluated as hybrid assemblies with joint reinforced pastes (JRP). JRP solder pastes form a resin fillet that gels around individual solder joints as the solder solidifies. In all cases, SAC305 BGA assemblies were used as the performance baseline.

Metallographic cross-sectional analysis of failed samples from all 7 test legs, across both thermal cycle profiles, revealed thermal fatigue cracking in the bulk solder, primarily at the package side of the solder joint. A much smaller amount of fatigue cracking was detected in the Bi-mixed region of hybrid and JRP solder joints. Fatigue cracking at the package side is the predominant failure location. Fatigue cracking at the package side in the SAC region is characterized by local recrystallization, global recrystallization, crack branching, and cavitation at boundary triple points. The fatigue cracking at the PCB side in the Bi-mixed region proceeds typically along phase boundaries, recrystallized Sn grains, and occasionally by cleavage through Bi precipitates. Backscattered SEM analysis showed no significant Bi precipitation in the vicinity of the package-side cracking, even in hybrid Sultan 2, the hybrid assembly with the highest initial Bi mixing level. However, when Bi is present in a solid solution, it is expected to affect thermal fatigue performance, but dissolved Bi cannot be detected with backscattered imaging.

The CABGA192 component was affected differently across the 0/100 °C and -15/85 °C thermal cycling profiles. From a characteristic lifetime analysis, all the low temperature solder test legs, across both ATC profiles, were shown to have a characteristic lifetime performance equivalent to the SAC baseline, with one exception; the homogeneous Red Flesh leg as run in the 0/100 °C profile. However, this performance delta went away when this leg was run in the less aggressive -15/85 °C profile. When looking at the thermal cycle profile ratio comparisons for characteristic lifetime, all test legs were extended beyond the SAC baseline in the less aggressive -15/85 °C profile, except for the Hybrid Sultan 2 and the Hybrid Golden Pillow 2 JRP, which showed a decrease in the ratio. One hypothesis for the lower hybrid solder joint performance difference versus SAC could be the occurrence of the ball drift mechanism (solderballs shifting out of their position during thermal cycling, potentially increasing the solder joint strain within the unmelted SAC region with increasing number of thermal cycles). Additionally, the Golden Pillow 2 JRP performance may be influenced by HoP or partial HoP defects generated during the reflow soldering process (i.e., at Time Zero), which might also account for the Golden Pillow 2 JRP performance difference versus SAC.

From a 1% cumulative failure analysis, the homogeneous Red Flesh and homogeneous Sultan 2 were shown to have relatively lower performance as compared with the SAC305 baseline in the 0/100 °C profile. However, this performance delta went away when these legs were run in the less aggressive -15/85 °C profile. It was also observed that for both the Beserah JRP and Golden Pillow 2 JRP as run in the less aggressive -15/85 °C profile, there was relatively lower 1% cumulative failure as compared to both the 0/100 °C profile and to the SAC305 baseline. This finding was also observed when looking at the thermal cycle profile ratio comparisons for 1% cumulative failure.

As this JRP behavior was not observed with the 0/100 °C profile, it suggests that earlier 1% cumulative failure values for resin reinforced material properties may be more sensitive to the colder temperatures found in the -15 °C to 0 °C temperature range, or it may be possible that the resins are not adhering as firmly to the solder mask or solder joint at -15 °C as they do at 0 °C. To validate these hypotheses, additional JRP experiments (including but not limited to nano-hardness evaluations) should be conducted to determine the impact of thermal cycling temperatures below 0 °C on resin reinforcement materials. As resin reinforcement is shown to be effective in resisting fatigue damage for greater characteristic life performance, the potential effects of other variables should be considered. It should be noted that other factors may also influence the reliability performance of resin reinforcement, such as the differences in the JRP test legs of alloy composition, reflow profile, Bi mixing level (Figure 8), microstructure, and resin chemistry and properties.

Cross-sectional analysis also detected multiple examples of the deformation phenomenon known as solder ball drift. Solder ball drift was detected at inner and outer row sites, was not limited to high strain locations, and occurred with both hybrid reflow profiles. Solder ball drift occurred more frequently, and the deformation was more severe with the CABGA192 than with the CTBGA84. Solder ball drift was not found in hybrid (heterogeneous) assemblies prior to thermal cycling and was not found in homogeneous LTS or SAC assemblies. Despite the extent of the deformation, solder ball drift seldom resulted in an open circuit failure in the solder joint and was not considered a primary failure mode in this investigation.

FUTURE WORK

The -15/85 °C thermal profile cycling work will be completed on the CTBGA84 component to determine the characteristic lifetimes, solder joint failure modes and failure locations in the solder joint. This data will be compared to the CTBGA84 data from the 0/100 °C thermal profile cycling results. Comparable failure analysis and data analysis will be performed, and the results will be reported later.

ACKNOWLEDGEMENTS

The iNEMI LTSPD project achievements rely heavily on the engagement, great effort and contribution of the whole participating project team members. These members include engineers from the following corporations: Intel, Celestica, Wistron, IBM, Lenovo, Nokia, HP, Flex, Indium, Senju, MacDermid Alpha Electronics Solutions, Interflux, Eunow, Shinko Electric Industries, Nihon Superior, Heraeus, Dell, Keysight, Abbott, Safran, Binghamton University, and Purdue University. The LTSPD Project Team also acknowledges the in-kind contribution of materials, components, and PCBs to our project from ASE, FIT, ITEQ, Lotes, Molex, Panasonic, Tamura, Tripod, Yincae, Shengyi Technology and Shengyi Electronics. iNEMI also acknowledges the contributions for accelerated temperature cycling, test monitoring, and analytical support from the management of Nokia Bell Labs in Murray Hill, NJ and the management of Intel's CQN Lab in Folsom, CA and Intel's Failure Analysis Lab in Hillsboro, OR.

REFERENCES

[1] Shubhada Sahasrabudhe, Scott Mokler, Mukul Renavikar, Sandeep Sane, Kevin Byrd, Eric Brigham, Owen Jin, Pubudu Goonetilleke, Nilesh Badwe and Satish Parupalli, "Low Temperature Solder – A Breakthrough Technology for Surface Mounted Devices," *Proceedings 68th Electronic Components and Technology Conference*, 1455-1464, San Diego, CA, May 29-June 1, 2018.

[2] R. Aspandiar, K. Byrd, K.K. Tang, L. Campbell, and S. Mokler, "Investigations of Low Temperature Solders to Reduce Reflow Temperature, Improve SMT Yields and Realize Energy Savings," *Proceedings of the 2015 APEX Conference*, San Diego, CA, February 2015.

[3] Scott Mokler, Raiyo Aspandiar, Kevin Byrd, Olivia Chen, Satyajit Walwadkar, Kok Kwan Tang, Mukul Renavikar and Sandeep Sane, "The Application of Bi-Based Solders for Low Temperature Reflow to Reduce Cost while Improving SMT Yields in Client Computing System, *Proceedings of SMTAI 2016*, 318-326, Rosemont, IL, September 2016.

[4] Max Hansen, **Constitution of Binary Alloys**, 2nd edition, McGraw-Hill, 1175-1177, 1958.

[5] H. Kang, S. H. Rajendran, J. P. Jung, "Low Melting Temperature "Sn-Bi Solder: Effect of Alloying and Nanoparticle Addition on the Microstructural, Thermal, Interfacial Bonding, and Mechanical Characteristics." *Metals* 11, 364, 2021.

[6] Raiyo Aspandiar, Nilesh Badwe, and Kevin Byrd, "Chapter 5: Low Temperature Lead-Free Alloys and Solder Pastes," **in Lead-free Soldering Process Development and Reliability**, Jasbir Bath, editor, 95-154, John Wiley & Sons, Inc. Print July 28, 2020, ISBN 9781119482031, online July 3, 2020, ISBN 9781119482093.

[7] Y. Liu and K.N. Tu, "Low melting point solders based on Sn, Bi, and In elements," *Materials Today Advances*, 1-16, 8, 100115, 2020.

[8] Fengjiang Wang, Hong Chen, Yiang Huang, Luting Liu, and Zhijie Zhang, "Recent progress on the development of Sn-based low-temperature Pb-free solders," *J. Materials Science: Materials in Electronics*, 30, 3222-3243, 2019.

[9] Morgana Ribas, Tom Hunsinger, Traian Cucu, Ramakrishna H V, Garian Lim and Mike Murphy, **The Printed Circuit Assembler's Guide to Low-Temperature Soldering**, I-Connect007, eBook ISBN: 978-0-9998648-4-5, © 2018 BR Publishing, Inc., Rohnert Park, CA 94927, U.S.A.

[10] Hiren R. Kotadia, Philip D. Howes, Samjid H. Mannan, "A review: On the development of low melting temperature Pb-free solders," *Microelectronics Reliability*, 54, 1253-1273, 2014.

[11] F. Hua, Z. Mei and J. Glazer, "Eutectic Sn-Bi as an Alternative as to Pb-Free Solders", Proceedings of the IEEE Electronic Components and Technology Conference (ECTC), 277-283. 1998

[12] NCMS Report 0401RE96, "Lead-Free Solder Project – Final Report", National Center for Manufacturing Sciences (NCMS), August 1997.

[13] K-W. Moon, W.J. Boettinger, U.R. Kattner, C.A. Handwerker, D-J Lee, "The Effect of Pb Contamination on the Solidification Behavior of Sn-Bi Solders", J. Electron. Mater., 30(1), 45-52. 2001,

[14] J. Glazer, "Microstructure and Mechanical Properties of Pb-Free Solder Alloys for Low-Cost Electronic Assembly" A Review". J. Electron. Mater., 23(8), 1994, pp. 693-700.

[15] E. Ferrer, H. Holder, "57Bi-42Sn-1Ag: A Lead Free, Low Temperature Solder for the Electronic Industry," IPC

JEDEC 4th International Conference on Lead-Free Electronic Components and Assemblies, San Jose, CA, March 22-25, 2003.
[16] J. Wang, L. Wen, J. Zhou, and M. Chung, "Mechanical Properties and Joint Reliability Improvement of Sn-Bi Alloy," *Proceedings of the IEEE Electronic Components and Technology Conference (ECTC)*, 492-496, 2011.
[17] O. H. Chen, K. Byrd, S. Mokler, K. K. Tang, and R. Aspandiar, "Comparison Of The Mechanical Shock/Drop Reliability Of Flip Chip BGA (FCBGA) Solder Joints Formed By Soldering With Low Temperature BiSn-Based Resin Reinforced Solder Pastes," *Proceedings of the 2015 International Conference on Soldering and Reliability (ICSR)*, Toronto, Canada, May 2015.
[18] O. H. Chen, A. Molina, R. Aspandiar, K. Byrd, S. Mokler, and K. K. Tang, "Mechanical Shock and Drop Reliability Evaluation of the BGA Solder Joint Stack-Ups Formed by Reflow Soldering SAC Solder Balls BGAs With BiSnAg And Resin Reinforced BiSn-Based Solder Pastes," *Proceedings of the 2015 SMTA International Conference*, 215-222, Rosemont, IL, September 2015.
[19] O. H. Chen, J. Gao, T. C.C. Pan, K. K. Tang, R. Aspandiar, K. Byrd, B. Zhou, S. Mokler, and A. Molina, "Solder Joint Reliability on Mixed SAC-BiSn Ball Grid Array Solder Joints Formed with Resin Reinforced Bi-Sn Metallurgy Solder Pastes," *Proceedings of the 2016 SMTA International Conference*, 216-228, Rosemont, IL, September 2016.
[20] R. Coyle, R. Aspandiar, M. Osterman, C. Johnson, R. Popowich, R. Parker and D. Hillman, "Thermal Cycle Reliability of a Low Ag Ball Grid Array Assembled with Tin Bismuth Solder Paste," *Proceedings of 2017 SMTA International Conference*, 72-83, Rosemont, IL, September 2017.
[21]https://news.lenovo.com/pressroom/press-releases/lenovo-announces-breakthrough-innovative-pc-manufacturing-process/ Lenovo™ Announces Breakthrough, Innovative PC Manufacturing Process.
[22] Haley Fu, Jagadeesh Radhakrishnan, Pubudu Goonetilleke, Kei Murayama, Raiyo Aspandiar, Babak Arfaei, Kevin Byrd, Antonio Caputo, Jimmy Chen, Qin Chen, Richard Coyle, Derek Daily, Sophia Feng, Carol Handwerker, Ralph Lauwaert, Francis Mutuku, Morgana Ribas, Murali Sarangapani, Kok Kwan Tang, Kris Troxel, Vasu Vasudevan, Daniel Werkhoven, Greg Wu, Hongwen Zhang, Wilson Zhen, "iNEMI Project on Process Development of BiSn-based low temperature solder pastes - Part VII: Mechanical Shock Test and Failure Analysis on Mixed SnAgCu-BiSn Solder Joints of FCBGA Components," *Proceedings of the 2020 SMTA International Virtual Conference*, September 2020.
[23] M. Ribas, P. Augustine, P. Choudhury, R.R. Rangaraju, A. Kumar, S. Sarkar, "Low Temperature Soldering: Thermal Cycling Reliability Performance," *Proceedings of the 2019 APEX Conference,* S05-02, San Diego, CA, February 4-6, 2019.
[24] H. Fu, J. Radhakrishnan, M. Ribas, R. Aspandiar, B. Arfaei, K. Byrd, A. Caputo, J. Chen, S. Cheng, Q. Chen, R. Coyle, D. Daily, S. Feng, P. Goonetilleke, R. Lauwaert, F. Mutuku, M. Sarangapani, K. K. Tang, K. Troxel, D. Werkhoven, G. Wu, A. Zhang, W. Zhen, "iNEMI Project on Process Development of BiSn-based low temperature solder pastes - Part VI: Mechanical Shock Results of Resin Reinforced Mixed SnAgCu-BiSn Solder Joints of FCBGA Components", *Proceedings of the 2019 SMTA International Conference*, Rosemont, IL, October 2019.
[25] Pritha Choudhury, Morgana Ribas, Raghu Raj Rangaraju and Siuli Sarkar, "High Reliability Low Temperature Solder Alloys, " *Proceedings of the 2019 SMTA International Conference,* Rosemont, IL, October 2019.
[26] H. Fu, J. Radhakrishnan, M. Ribas, R. Aspandiar, K. Byrd, J. Chen, S. Cheng, Q. Chen, R. Coyle, S. Feng, B. Hardin, M. Krmpotich, S. Mokler, B. Sandy-Smith, K. K. Tang, G. Wu, A. Zhang, and W. Zhen, "iNEMI Project on Process Development of BiSn-Based Low Temperature Solder Pastes – Part III: Mechanical Shock Tests on POP BGA Assemblies", *Proceedings of the 2018 International Conference on Electronics Packaging (IECP)*, Kuwana, Japan, April, 2018.
[27] M. Ribas, S. Chegudi, A. Kumar, R. Pandher, R. Raut, S. Mukherjee, S. Sarkar, and B. Singh, "Development of Low-Temperature Drop Shock Resistant Solder Alloys for Handheld Devices," *Proceedings of the IEEE 15th Electronics Packaging Technology Conference*, 53-57, Singapore. December 2013.
[28] Chongyang Cai, Jiefeng Xu, Huayan Wang, S.B. Park, "A comparative study of thermal fatigue life of Eutectic Sn-Bi, Hybrid Sn-Bi/ SAC and SAC solder alloy BGAs," *Microelectronics Reliability*, vol. 119, 2021. https://doi.org/10.1016/j.microrel.2021.114065.
[29] Charmaine Johnson, Richard Coyle, Martin Anselm, Lenora Clark, Ajitesh Singh Parihar, Richard Popowich, Tayler Swanson, Jason Fullerton, and Chen Xu, "Attachment Quality and Thermal Fatigue Reliability of a Surface Mount Chip Resistor Assembled with a Low Temperature Solder," *Proceedings of SMTAI*, 457-464, Rosemont, IL, September 2019.
[30] Richard Coyle, Martin Anselm, Faramarz Hadian, Sahana Kempaiah, Anto Raj, Richard Popowich, Lenora Clark, Jason Fullerton, and Charmaine Johnson, "The Effect of Peak Reflow Temperature on Thermal Cycling Performance and Failure Mode of Hybrid Low Temperature Solder Joints," *Proceedings of SMTAI 2021*, 386-399, Minneapolis, MN, November 2021.
[31] Luke Wentlent, James Wilcox, and Michael Meilunas, "Thermal Cycling Behaviors of Hybrid and Homogeneous Low Temperature Solder Interconnects," *Proceedings of SMTAI 2021*, 547-563, Minneapolis, MN, November 2021.

[32] Sahana Marur Kempaiah, Martin K Anselm, Richard Coyle, and Faramarz Hadian, "Thermal Reliability of Mixing Bismuth-Containing Solder Paste with SAC BGAs at Low Reflow Temperatures - Part II," *Proceedings of SMTAI 2021*, 478-485, Minneapolis, MN, November 2021.
[33] Andrew Mawer, Mollie Benson, A.R. Nazmus Sakib, Nihaar Mahatme, Anirban Roy, Paul Ngan, and Catherine Pronga, "Hybrid Assembly and Reliability of Conventional Pb-Free BGAs Using Low Temperature Solder Paste for Temperature Sensitive IC Applications," *Proceedings of SMTAI 2021*, 486-494, Minneapolis, MN, November 2021.
[34] Kevin Byrd, Jason Stafford, Prithvi Kotian, Pubudu Goonetilleke, and Brian Franco, "SAC-SnBi Solder Joint Failure Location vs. Acceleration Condition," *Proceedings of SMTAI 2021*, 366-371, Minneapolis, MN, November 2021.
[35] Haley Fu, Raiyo Aspandiar, Jimmy Chen, Shunfeng Cheng, Qin Chen, Richard Coyle, Sophia Feng, Bill Hardin, Mark Krmpotich, Scott Mokler, Jagadeesh Radhakrishnan, Morgana Ribas, Brook Sandy-Smith, Kok Kwan Tang, Greg Wu, Anny Zhang, Wilson Zhen, "iNEMI Project on Process Development of BiSn-Based Low Temperature Solder Pastes *Proceedings of SMTA International*, 207-220, September 7 - 21, 2017, Rosemont, IL.
[36] Haley Fu, Raiyo Aspandiar, Jimmy Chen, Shunfeng Cheng, Qin Chen, Richard Coyle, Sophia Feng, Bill Hardin, Mark Krmpotich, Scott Mokler, Jagadeesh Radhakrishnan, Morgana Ribas, Brook Sandy-Smith, Kok Kwan Tang, Greg Wu, Anny Zhang, Wilson Zhen, "iNEMI Project on Process Development of BiSn-Based Low Temperature Solder Pastes: Characterization of Mixed Alloy BGA Solder Joints, *Proceedings of Pan Pacific Microelectronics Symposium*," February 5-8, 2018, Hawaii, HI.
[37] Richard Coyle, Raiyo Aspandiar, Faramarz Hadian, Sahana Kempaiah, Vasu Vasudevan, Aileen Allen, Anto Raj, Pubudu Goonetilleke, Dan Burkholder, Morgana Ribas, Jagadeesh Radhakrishnan, Carol Handwerker, Hongwen Zhang, Babak Arfaei, Haley Fu, Qin Chen, Derek Daily, Ralph Lauwaert, Francis Mutuku, Kei Murayama, Murali Sarangapani, Daniel Werkhoven, "Interim Thermal Cycling Report on Hybrid and Homogeneous LTS Solder Joints," *Proceedings of SMTAI 2021*, 400-425, Minneapolis, MN, November 2021.
[38] Gregory Henshall, Keith Sweatman, Keith Howell, Joe Smetana and Richard Coyle, Richard Parker, Stephen Tisdale, Fay Hua, Weiping Liu, Robert Healey, Ranjit S. Pandher, Derek Daily, Mark Currie, Jennifer Nguyen, "iNEMI Lead-Free Alloy Alternatives Project Report: Thermal Fatigue Experiments and Alloy Test Requirements," *Proceedings of SMTAI*, 317-324, San Diego CA, 2009.
[39] Amkor Technology Datasheets: CABGA DS550T (Rev. 11/15) and CTBGA DSS550N (Rev. 1/07), Amkor Technology, www.amkor.com, Tempe, AZ.
[40] R. Aspandiar, N. Badwe, K. Byrd, K.K. Tang, L. Campbell and S. Mokler, "Investigation of Low Temperature Solders to Reduce Reflow Temperature, Improve SMT Yields and Realize Energy Savings," *Proceedings of the 2015 APEX Conference*, San Diego, CA, S14-03, February 2015.
[41] Richard Coyle, Dave Hillman, Richard Parker, Charmaine Johnson, Michael Osterman, Jasbir Bath, Babak Arfaei, Andre Delhaise, Keith Howell, Brook Sandy-Smith, Joe Smetana, Stuart Longgood, "The Effect of Bismuth, Antimony, or Indium on the Thermal Fatigue of High Reliability Pb-Free Solder Alloys," *Proceedings of SMTAI*, Rosemont, IL, October 2018.
[42] Richard Coyle, Dave Hillman, Charmaine Johnson, Richard Parker, Brook Sandy-Smith, Hongwen Zhang, Jie Geng, Michael Osterman, Babak Arfaei, Andre Delhaise, Keith Howell, Jasbir Bath, Joe Smetana, Stuart Longgood, Andre Kleyner, Julie Silk, Ranjit Pandher, Eric Lundeen, and Jerome Noiray "Alloy Composition and Thermal Fatigue of High Reliability Pb-Free Solder Alloys," *Proceedings of SMTAI*, Rosemont, IL, October 2018.
[43] Richard Coyle, Charmaine Johnson, Dave Hillman, Richard Parker, Michael Osterman, Joe Smetana, Tim Pearson, Babak Arfaei, Keith Howell, Stuart Longgood, Andre Kleyner, Julie Silk, Andre Delhaise, Hongwen Zhang, Jie Geng, Ranjit Pandher, Eric Lundeen, "Thermal Cycling Reliability and Failure Mode of Two Ball Grid Array Packages with High Reliability Pb-Free Solder Alloys," *Proceedings of SMTA International*, 436-456, September 22-26, 2019, Rosemont, IL.
[44] IPC-9701B, "Thermal Cycling Test Method for Fatigue Life Characterization of Surface Mount Attachments," IPC, Bannockburn, IL, 2021.
[45] W.D. McCallister, Materials Science and Engineering: An Introduction, John Wiley & Sons, 2003, Chap 7.
[46] L. Coffin, Jr., Met. Eng. Q., Vol 3, p. 15 (1963).
[47] S. Manson, Thermal Stress and Low-Cycle Fatigue, McGraw-Hill, New York (1966).
[48] K.C. Norris and A. H. Landzberg, "Reliability of Controlled Collapse Interconnections," IBM J. Res. Dev., Vol. 13, No. 3, pp. 266-271 (1969).
[49] W. Engelmaier, "Fatigue Life of Leadless Chip Carrier Solder Joints During Power Cycling", IEEE Transactions on Components, Hybrids, and Manufacturing Technology, vol.6, no.3, pp. 232-237, September 1983
[50] F. Hadian, M. Genanu, R. Owen, and E. J. Cotts, "The dependence of the microstructure of SnAgCu/SnBiAg mixed assemblies on reflow temperature," in Proceedings of SMTA International, 2020, pp. 326–332.
[51] M. Genanu, F. Hadian, R. Owen, and E. J. Cotts, "The effect of thermal history on the microstructure of SnAgCu/SnBiAg mixed assemblies," J. Electron. Mater., no. In Press, 2020, doi: https://doi.org/10.1007/s11664-020-08474-3.

[52] “ImageJ: Image Processing and Analysis in Java,” https://imagej.nih.gov/ij/index.html
[53] S. A. Belyakov J. Xian, G. Zeng, K. Sweatman, T. Nishimura, T. Akaiwa, C. M. Gourlay., “Precipitation and coarsening of bismuth plates in Sn–Ag–Cu–Bi and Sn–Cu–Ni–Bi solder joints,” J. Mater. Sci. Mater. Electron., vol. 30,
[54] S. Dunford, S. Canumalla, and P. Viswanadham, “Intermetallic Morphology and Damage Evolution Under Thermomechanical Fatigue of Lead (Pb)-Free Solder Interconnections,” *Proceedings of Electronic Components Technology Conference,* 726-736, Las Vegas, NV, June 1-4, 2004.
[55] Liang Yin, Luke Wentlent, Linlin Yang, Babak Arfaei, Awni Oasaimeh, and Peter Bargemen, “Recrystallization and Precipitate Coarsening in Pb-Free Solder Joints During Thermomechanical Fatigue,” J. Electronic Materials, Vol. 41, No. 2, 241-252, 2011.
[56] Babak Arfaei, Francis Mutuku, Richard Coyle, Eric Cotts, and Jim Wilcox, “Failure Mechanism and Microstructural Evolution of Pb-free Solder Alloys in Thermal Cycling Tests: Effect of Solder Composition and Sn Grain Morphology,” *Proceedings 65th Electronic Components and Technology Conference*, 118-126, 2015.
[57] André Delhaise, “Solid-State Diffusion of Bismuth in Tin-Rich , Lead-Free Solder Alloys,” A thesis submitted in conformity with the requirements for the degree of Doctor of Philosophy, Department of Materials Science & Engineering University of Toronto, 67, 2018
[58] David A. Porter, Kenneth E. Easterling, and Mohammed Y. Sherif, **Phase Transformations in Metals and Alloys**, Third Edition, 112, CRC Press Taylor, 2009.
[59] J. W. Morris, Jr, J. L. Freer Goldstein, and Z. Mei, ‘‘Microstructural Influences on the Mechanical Properties of Solder’’, in **The Mechanics of Solder Alloy Interconnects**, edited by D. Frear, H. Morgan, S. Burchett, and J. Lau, Van Nostrand Reinhold, New York, 1994.
[60] L. Wentlent, J. Wilcox, and M. Meilunas, “Reliability Behavior of Surface Mount Devices Assembled with Bismuth Bearing Low-Melt Solder Pastes,” *Proceedings of SMTAI Virtual,* 442-450, September 28- October 23, 2020.

APPENDIX A

Relevant Board Assembly Parameters

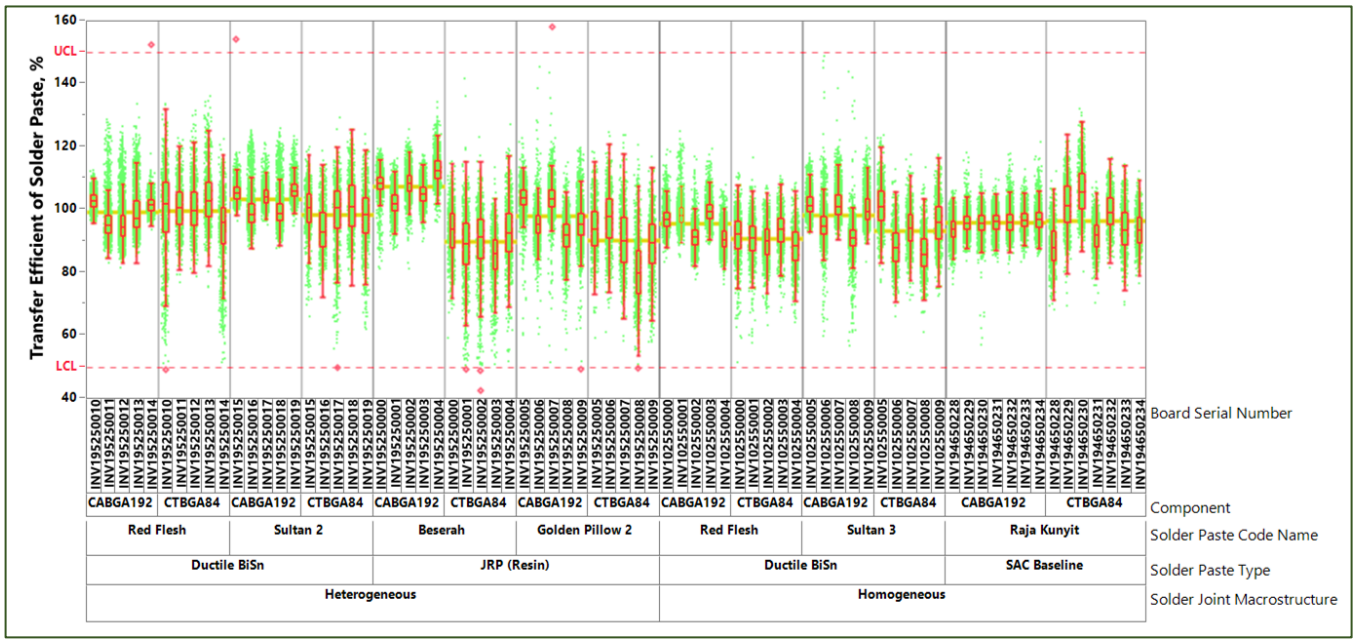

Figure A-1: Solder Paste Transfer Efficiency for Various Solder Pastes used in this study to assemble the Alloy ATC TV board [37].

Oven Name: BTU01 Process Window Name: INEMI ATC ALLOY TV_PS_64800-05

Setpoints (Degree Celsius)												
Zone	1	2	3	4	5	6	7	8	9	10	11	12
Top	150	155	170	175	180	180	185	210	230	265	265	230
Bottom	150	155	170	175	180	180	185	210	230	265	265	230
Conveyor Speed (cm/min):	92.0											

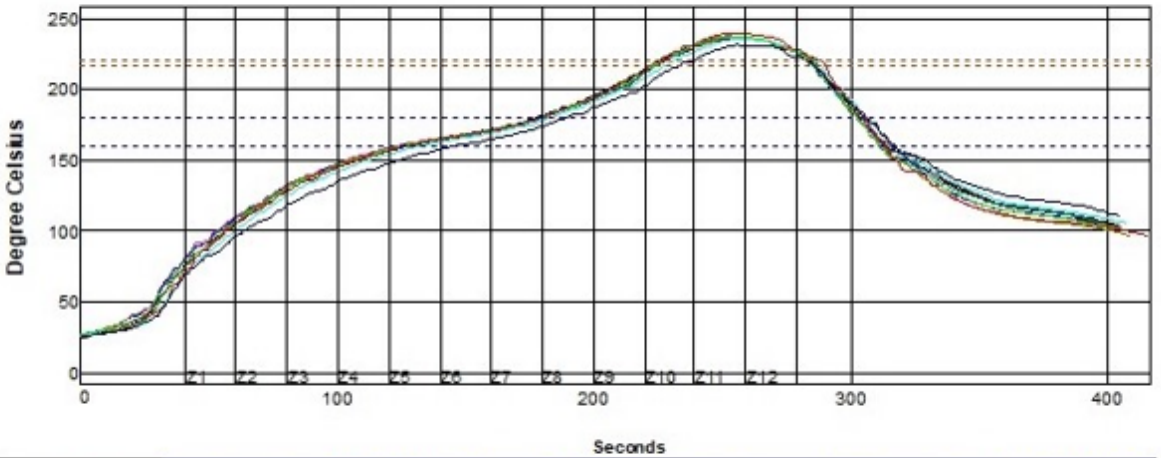

PWI = 202%	Max Rising Slope		Max Falling Slope		Soak Time 160-180°C		Peak Temp		Tot Time /217°C		Tot Time /220°C-2	
TC1	1.86	24%	-2.06	57%	55.48	40%	237.67	-49%	64.08	154%	59.87	98%
TC2	1.87	25%	-2.04	59%	53.07	8%	236.90	-54%	63.75	150%	59.23	90%
TC3	1.83	22%	-2.07	57%	54.68	29%	237.34	-51%	63.51	147%	59.32	91%
TC4	1.94	29%	-1.93	63%	52.76	4%	237.06	-53%	63.43	146%	59.28	90%
TC5	1.89	26%	-1.88	65%	52.67	2%	236.12	-59%	62.62	135%	58.21	76%
TC6	1.91	28%	-1.92	63%	54.62	28%	237.01	-53%	60.83	111%	56.37	52%
TC7	1.91	27%	-1.91	63%	50.40	-28%	235.45	-64%	60.27	104%	55.72	43%
TC8	1.96	31%	-2.06	58%	53.84	18%	237.28	-51%	63.27	144%	59.37	92%
TC9	1.95	30%	-2.27	49%	52.36	-2%	240.01	-33%	67.62	202%	64.26	157%
TC10	1.76	17%	-1.80	68%	43.59	-119%	231.23	-92%	52.33	-2%	44.72	-104%
Delta	0.20		0.47		11.89		8.78		15.29		19.54	

Figure A-2. Reflow Profile for the Raja Kunyit paste used in Leg #1, the SAC Baseline category [37].

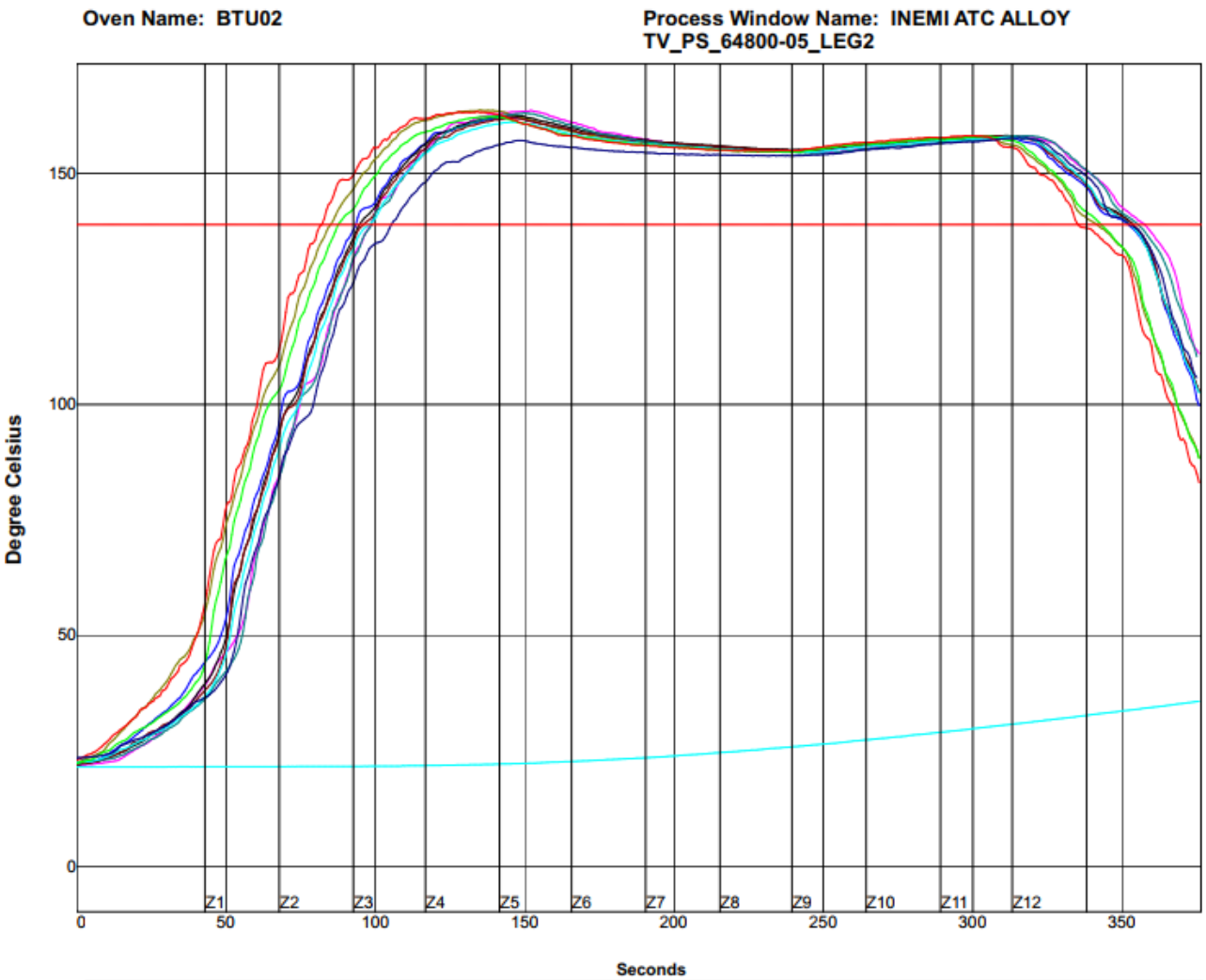

PWI= 88%	Max Rising Slope		Reflow Time /139°C		Peak Temp	
TC1	2.14	12%	258.95	-68%	163.73	75%
TC2	2.11	9%	258.44	-69%	162.23	45%
TC3	2.12	10%	256.60	-72%	163.78	76%
TC4	2.15	12%	259.08	-68%	162.73	55%
TC5	2.20	16%	257.53	-71%	162.12	42%
TC6	2.22	19%	256.60	-72%	163.17	63%
TC7	2.16	13%	254.92	-75%	161.23	25%
TC8	2.28	23%	255.42	-74%	162.45	49%
TC9	2.27	23%	253.26	-78%	163.45	69%
TC10	2.10	8%	247.14	-88%	157.78	-44%
Delta	0.18		11.94		6.00	

Figure A-3. Reflow Profile for the Beserah paste used in Leg #2, the JRP Resin category [37].

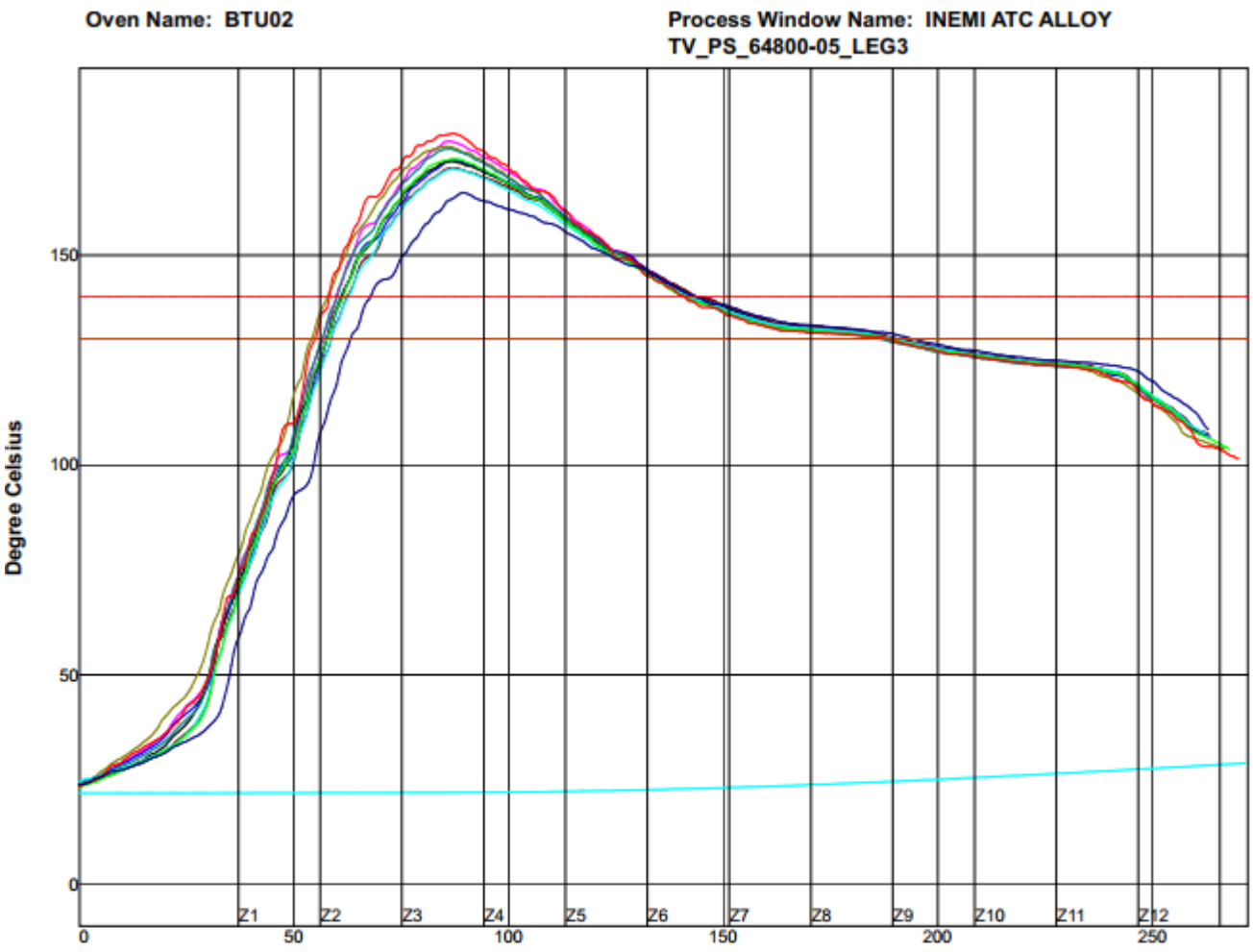

PWI= 168%	Max Rising Slope		Reflow Time /140°C		Peak Temp		Tot Time /130°C	
TC1	3.01	1%	82.89	129%	177.17	-4%	131.33	-87%
TC2	2.91	-9%	82.57	126%	172.67	-64%	133.38	-66%
TC3	2.90	-10%	83.51	135%	175.95	-21%	133.67	-63%
TC4	2.91	-9%	82.71	127%	172.45	-67%	132.77	-72%
TC5	2.93	-7%	82.52	125%	170.78	-90%	132.03	-80%
TC6	3.02	2%	81.18	112%	175.34	-29%	129.86	-101%
TC7	2.91	-9%	79.69	97%	170.56	-93%	131.04	-90%
TC8	3.04	4%	79.82	98%	172.95	-61%	130.83	-92%
TC9	3.12	12%	82.89	129%	179.01	20%	133.61	-64%
TC10	2.84	-16%	76.01	60%	164.90	-168%	130.73	-93%
Delta	0.28		7.50		14.11		3.81	

Figure A-4. Reflow Profile for the Golden Pillow 2 paste used in Leg #3, the JRP category [37].

Oven Name: BTU02 Process Window Name: INEMI ATC ALLOY TV_PS_64800-05_LEG4

Setpoints (Degree Celsius)												
Zone	1	2	3	4	5	6	7	8	9	10	11	12
Top	130	130	130	130	130	135	150	185	230	240	225	150
Bottom	130	130	130	130	130	135	150	185	230	240	225	150
Conveyor Speed (cm/min):	125.0											

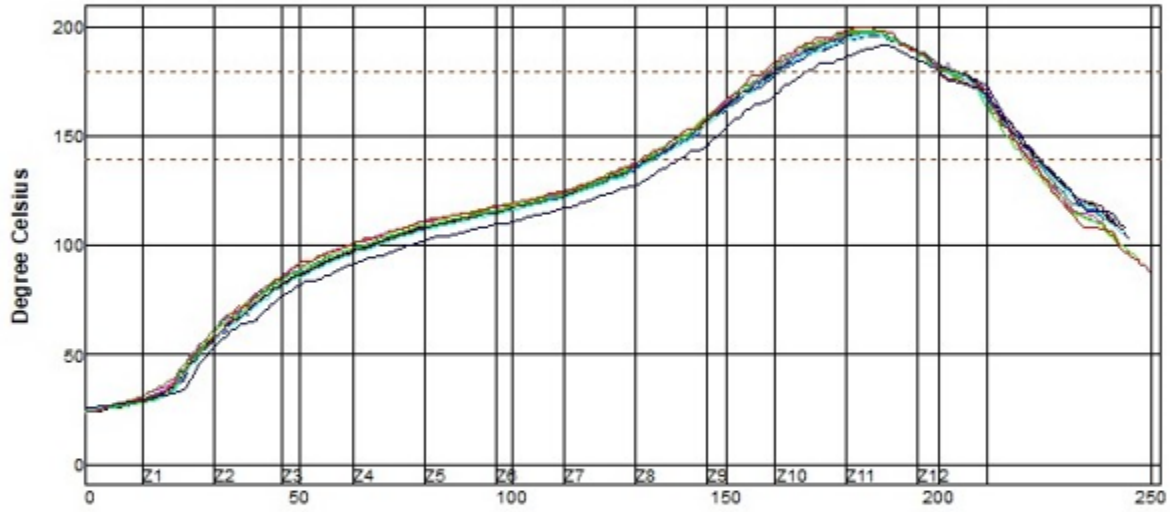

PWI= 106%	Max Rising Slope		Peak Temp		Tot Time /139°C		Tot Time /179°C-2	
TC1	1.68	-32%	197.73	55%	90.49	102%	44.55	-51%
TC2	1.63	-37%	195.51	10%	91.17	104%	40.95	-63%
TC3	1.65	-35%	198.28	66%	91.87	106%	42.45	-59%
TC4	1.65	-35%	197.28	46%	91.52	105%	43.56	-55%
TC5	1.65	-35%	196.06	21%	91.11	104%	42.82	-57%
TC6	1.66	-34%	197.56	51%	90.03	100%	43.51	-55%
TC7	1.66	-34%	196.28	26%	89.77	99%	40.55	-65%
TC8	1.72	-28%	197.78	56%	89.52	98%	42.66	-58%
TC9	1.76	-24%	199.56	91%	91.01	103%	41.22	-63%
TC10	1.53	-47%	191.45	-71%	84.22	81%	31.65	-94%
Delta	0.23		8.11		7.65		12.90	

Figure A-5. Reflow Profile for the Red Flesh paste used in Leg #4, the Hybrid (Heterogeneous) Ductile BiSn category [37].

Oven Name: BTU02 Process Window Name: INEMI ATC ALLOY TV_PS_64800-05_LEG5

Setpoints (Degree Celsius)												
Zone	1	2	3	4	5	6	7	8	9	10	11	12
Top	130	125	120	120	125	135	150	175	205	210	205	160
Bottom	130	125	120	120	125	135	150	175	205	210	205	160
Conveyor Speed (cm/min):	92.0											

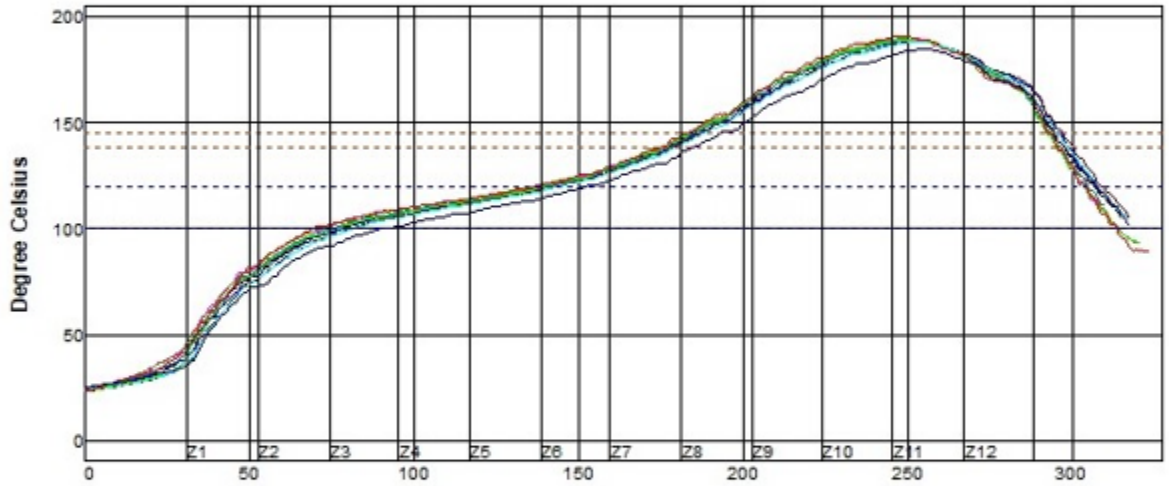

PWI= 118%	Max Rising Slope		Soak Time 100-120°C		Peak Temp		Tot Time /138°C		Tot Time /145°C-2	
TC1	1.54	2%	64.45	-70%	189.56	-30%	120.86	106%	109.51	30%
TC2	1.54	2%	62.19	-85%	188.12	-49%	122.00	113%	110.00	33%
TC3	1.53	2%	64.54	-70%	189.56	-30%	121.37	109%	109.77	32%
TC4	1.56	4%	62.41	-84%	189.28	-34%	122.63	118%	109.84	32%
TC5	1.58	5%	61.36	-91%	188.51	-44%	121.98	113%	109.80	32%
TC6	1.58	5%	64.88	-67%	189.45	-32%	119.61	97%	108.38	23%
TC7	1.57	5%	62.56	-83%	188.51	-44%	119.86	99%	107.62	17%
TC8	1.65	10%	63.00	-80%	189.23	-35%	120.41	103%	108.63	24%
TC9	1.60	6%	68.27	-45%	190.51	-19%	120.58	104%	110.96	40%
TC10	1.48	-5%	62.03	-86%	185.01	-87%	113.97	60%	101.84	-21%
Delta	0.17		6.91		5.50		8.66		9.12	

Figure A-6. Reflow Profile for the Sultan 2 paste used in Leg #5, the Hybrid (Heterogeneous) Ductile BiSn category [37].

Oven Name: BTU01

Process Window Name: INEMI ATC ALLOY TV_093_PS DP 5600 LMPA

Setpoints (Degree Celsius)												
Zone	1	2	3	4	5	6	7	8	9	10	11	12
Top	130	130	130	130	130	135	150	180	230	230	220	150
Bottom	130	130	130	130	130	135	150	180	230	230	220	150
Conveyor Speed (cm/min):	125.0											

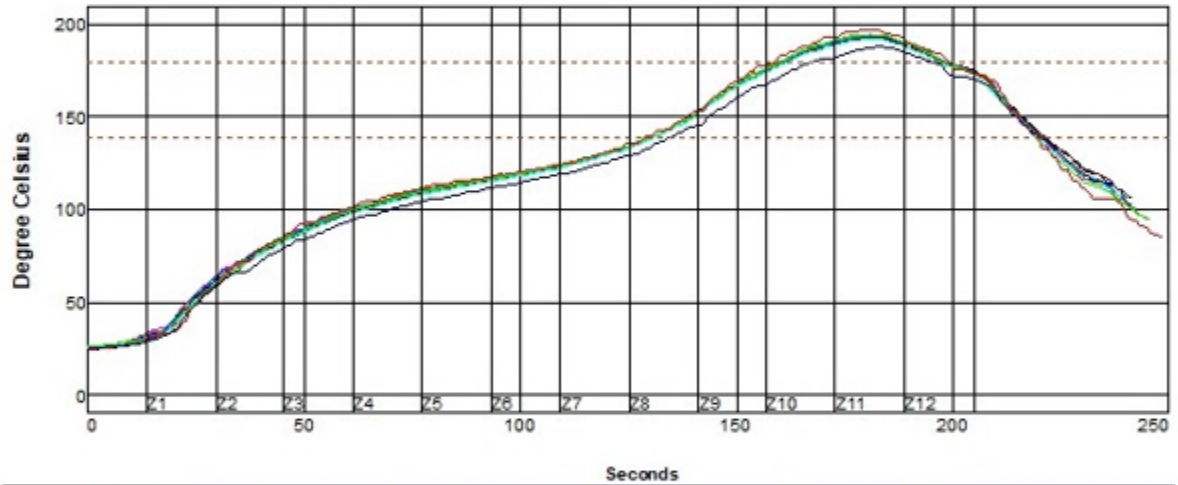

PWI= 145%	Max Rising Slope		Max Falling Slope		Peak Temp		Tot Time /139°C		Tot Time /179°C-2	
TC1	1.62	-38%	-1.95	37%	192.90	-42%	89.10	97%	38.02	-73%
TC2	1.64	-36%	-2.02	32%	192.56	-49%	89.82	99%	37.25	-76%
TC3	1.65	-35%	-2.08	28%	194.23	-15%	90.60	102%	38.80	-71%
TC4	1.68	-32%	-1.91	39%	193.34	-33%	91.11	104%	38.52	-72%
TC5	1.65	-35%	-1.90	40%	192.06	-59%	90.28	101%	36.87	-77%
TC6	1.67	-33%	-1.91	39%	193.90	-22%	89.48	98%	39.09	-70%
TC7	1.66	-34%	-1.91	39%	191.78	-64%	88.90	96%	35.49	-82%
TC8	1.71	-29%	-2.05	30%	194.28	-14%	89.10	97%	38.19	-73%
TC9	1.78	-22%	-2.26	16%	196.84	37%	90.72	102%	40.65	-65%
TC10	1.57	-43%	-1.82	45%	187.73	-145%	85.36	85%	28.79	-104%
Delta	0.21		0.44		9.11		5.75		11.86	

Figure A-7. Reflow Profile for the Red Flesh paste used in Leg #6, the Homogeneous Ductile BiSn category [37].

Oven Name: BTU01

Process Window Name: INEMI ATC ALLOY TV_093_PS DP 5600 LMPA

Setpoints (Degree Celsius)												
Zone	1	2	3	4	5	6	7	8	9	10	11	12
Top	135	130	125	120	122	135	155	190	210	210	210	170
Bottom	135	130	125	120	122	135	155	190	210	210	210	170
Conveyor Speed (cm/min):	98.0											

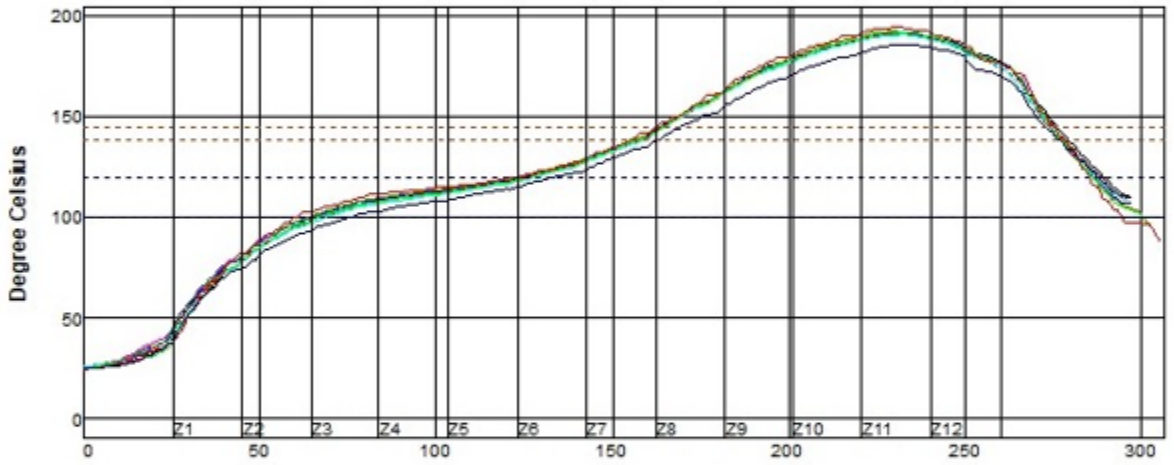

PWI= 138%	Max Rising Slope		Preheat 100-120°C		Peak Temp		Tot Time /138°C		Tot Time /145°C-2	
TC1	1.58	-42%	60.59	-96%	191.28	26%	119.12	91%	111.38	14%
TC2	1.63	-37%	59.72	-102%	191.73	35%	122.08	121%	111.87	19%
TC3	1.64	-36%	59.54	-103%	192.40	48%	123.58	136%	111.26	13%
TC4	1.66	-34%	59.31	-105%	191.95	39%	122.86	129%	111.48	15%
TC5	1.62	-38%	58.57	-110%	190.95	19%	121.25	113%	111.21	12%
TC6	1.64	-36%	61.94	-87%	190.73	15%	118.77	88%	109.17	-8%
TC7	1.65	-35%	58.91	-107%	190.51	10%	119.43	94%	109.85	-1%
TC8	1.71	-29%	59.72	-102%	192.06	41%	121.36	114%	109.69	-3%
TC9	1.77	-23%	63.94	-74%	194.40	88%	123.79	138%	111.63	16%
TC10	1.55	-45%	58.27	-112%	185.84	-83%	114.87	49%	102.97	-70%
Delta	0.22		5.67		8.56		8.92		8.90	

Figure A-8. Reflow Profile for the Sultan 2 paste used in Leg #7, the Homogeneous Ductile BiSn category [37].

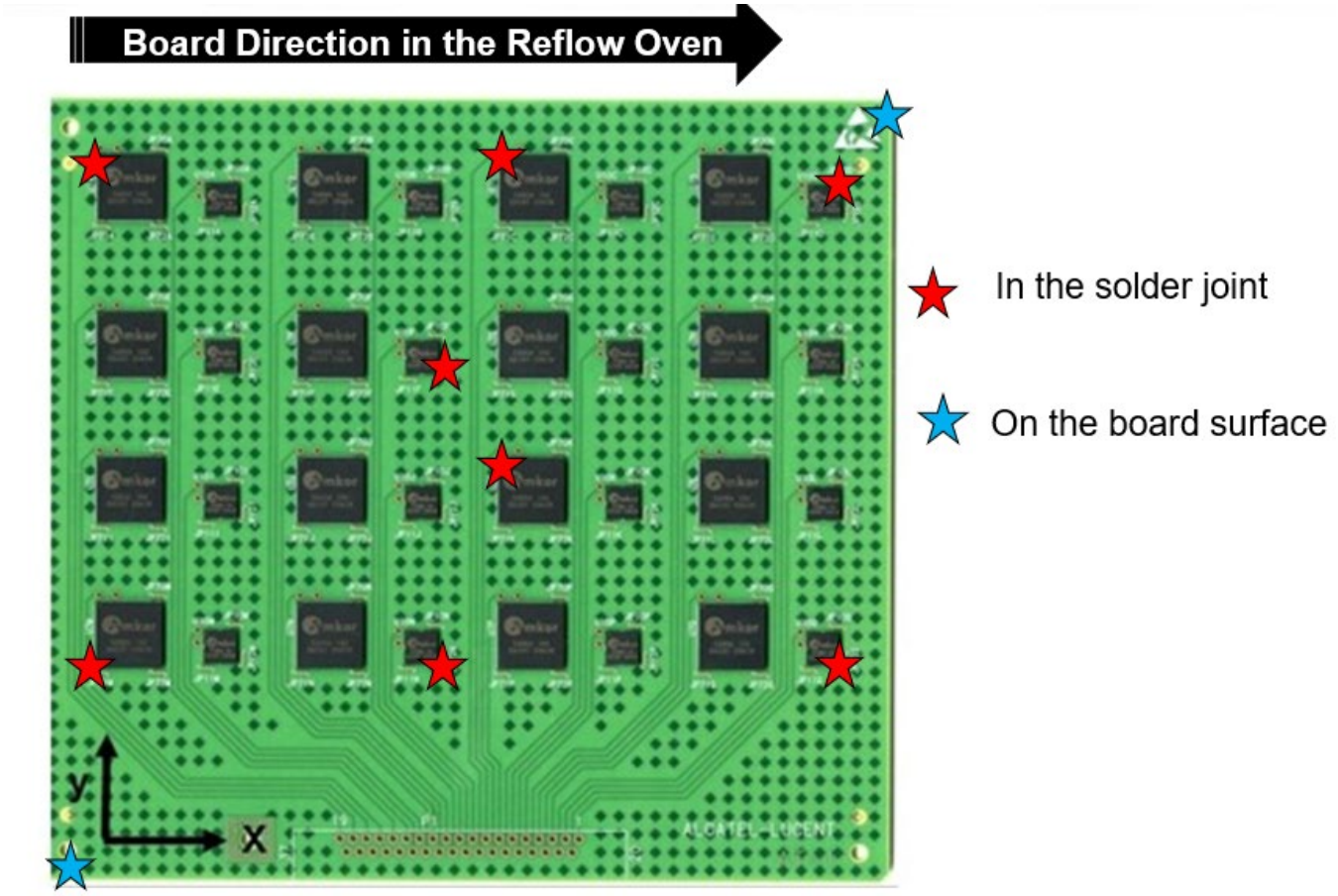

Figure A-9. The location of the thermocouples on the Alloy ATC TV board for measurement the Reflow Profiles of various experimental legs [37].

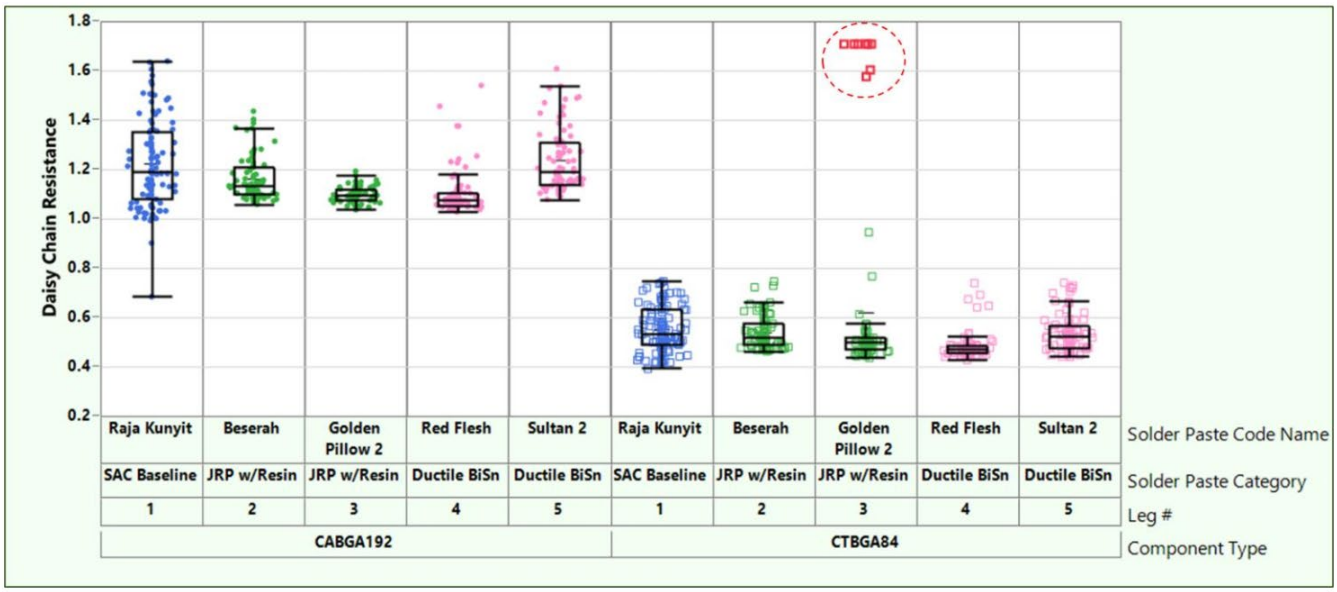

Figure A-10. Resistances of the Daisy Chains for the two Component Types on the Alloy ATC TV Boards after reflow soldering for all Legs in this Study [37].

Appendix B
Weibull Plots with 90% Confidence Intervals

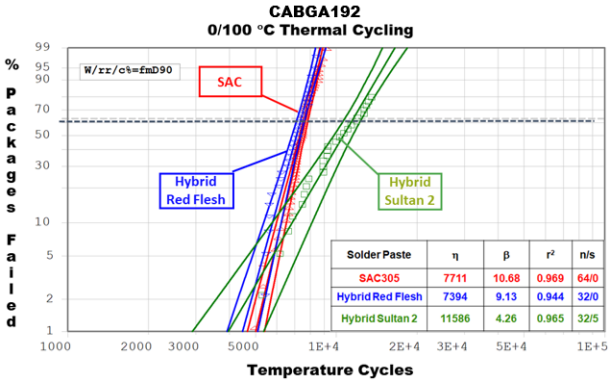

Solder Paste	η	β	r²	n/s
SAC305	7711	10.68	0.969	64/0
Hybrid Red Flesh	7394	9.13	0.944	32/0
Hybrid Sultan 2	11586	4.26	0.965	32/5

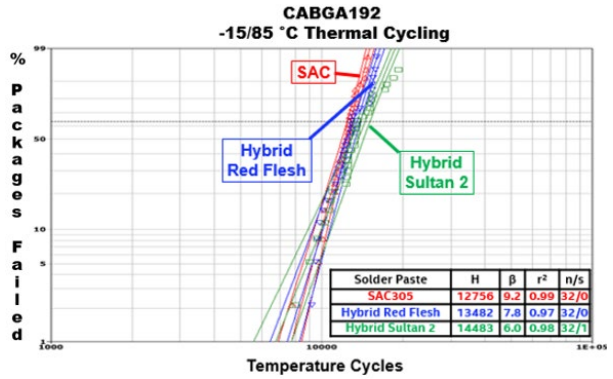

Solder Paste	H	β	r²	n/s
SAC305	12756	9.2	0.99	32/0
Hybrid Red Flesh	13482	7.8	0.97	32/0
Hybrid Sultan 2	14483	6.0	0.98	32/1

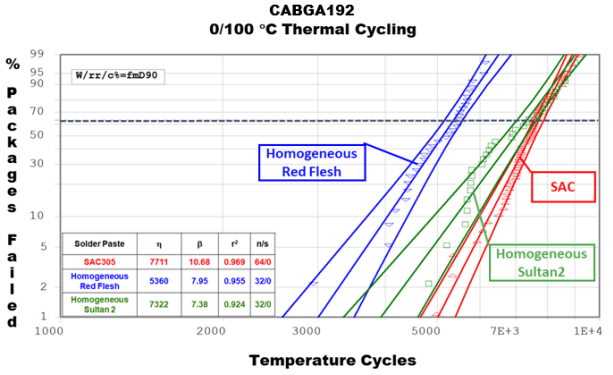

Solder Paste	η	β	r²	n/s
SAC305	7711	10.68	0.969	64/0
Homogeneous Red Flesh	5360	7.95	0.955	32/0
Homogeneous Sultan 2	7322	7.38	0.924	32/0

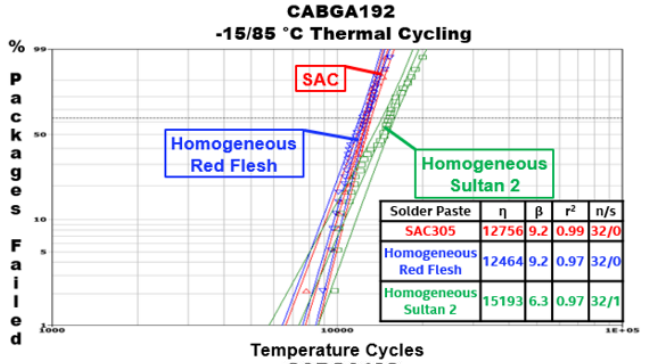

Solder Paste	η	β	r²	n/s
SAC305	12756	9.2	0.99	32/0
Homogeneous Red Flesh	12464	9.2	0.97	32/0
Homogeneous Sultan 2	15193	6.3	0.97	32/1

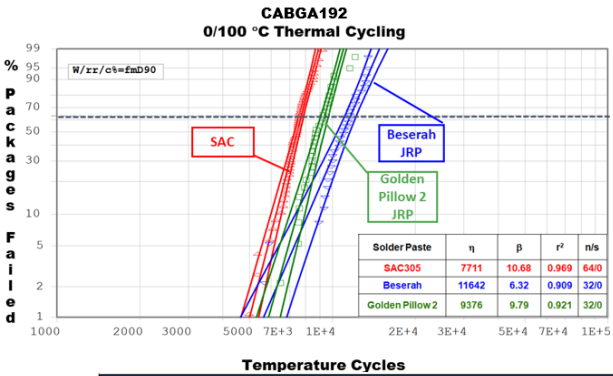

Solder Paste	η	β	r²	n/s
SAC305	7711	10.68	0.969	64/0
Beserah	11642	6.32	0.909	32/0
Golden Pillow 2	9376	9.79	0.921	32/0

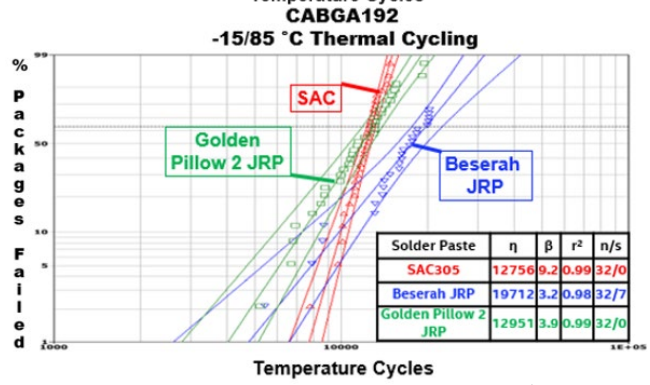

Solder Paste	η	β	r²	n/s
SAC305	12756	9.2	0.99	32/0
Beserah JRP	19712	3.2	0.98	32/7
Golden Pillow 2 JRP	12951	3.9	0.99	32/0

CABGA192 Weibull Statistics for 0/100 °C Thermal Cycling				
Solder Assembly Type	Characteristic Lifetime η (cycles)	1% Failures (cycles)	Slope β	Correlation Coefficient, r^2
SAC Baseline	7711	5012	10.7	0.97
Hybrid Red Flesh	7394	4468	9.1	0.94
Hybrid Sultan 2	11586	3931	4.3	0.96
Homogeneous Red Flesh	5360	3006	5.3	0.96
Homogeneous Sultan 2	7322	3925	7.4	0.92
Beserah Joint Reinforced Paste	11642	5624	7.4	0.92
Golden Pillow 2 Joint Reinforced Paste	9376	5860	9.8	0.92

CABGA192 Weibull Statistics for -15/85 °C Thermal Cycling				
Solder Assembly Type	Characteristic Lifetime η (cycles)	1% Failures (cycles)	Slope β	Correlation Coefficient, r^2
SAC Baseline	12756	7739	9.2	0.99
Hybrid Red Flesh	13482	7456	7.8	0.97
Hybrid Sultan 2	14483	6754	6.0	0.98
Homogeneous Red Flesh	12464	7559	9.2	0.97
Homogeneous Sultan 2	15193	7334	6.3	0.97
Beserah Joint Reinforced Paste	19712	4763	3.2	0.98
Golden Pillow 2 Joint Reinforced Paste	12951	4038	3.9	0.99

Note: The 0/100 °C thermal cycling profile Weibull plots and Weibull statistics data (above) were published previously [37].

Appendix C
X-ray Detection of Ball Drift in a CABGA192 (0/100°C profile)

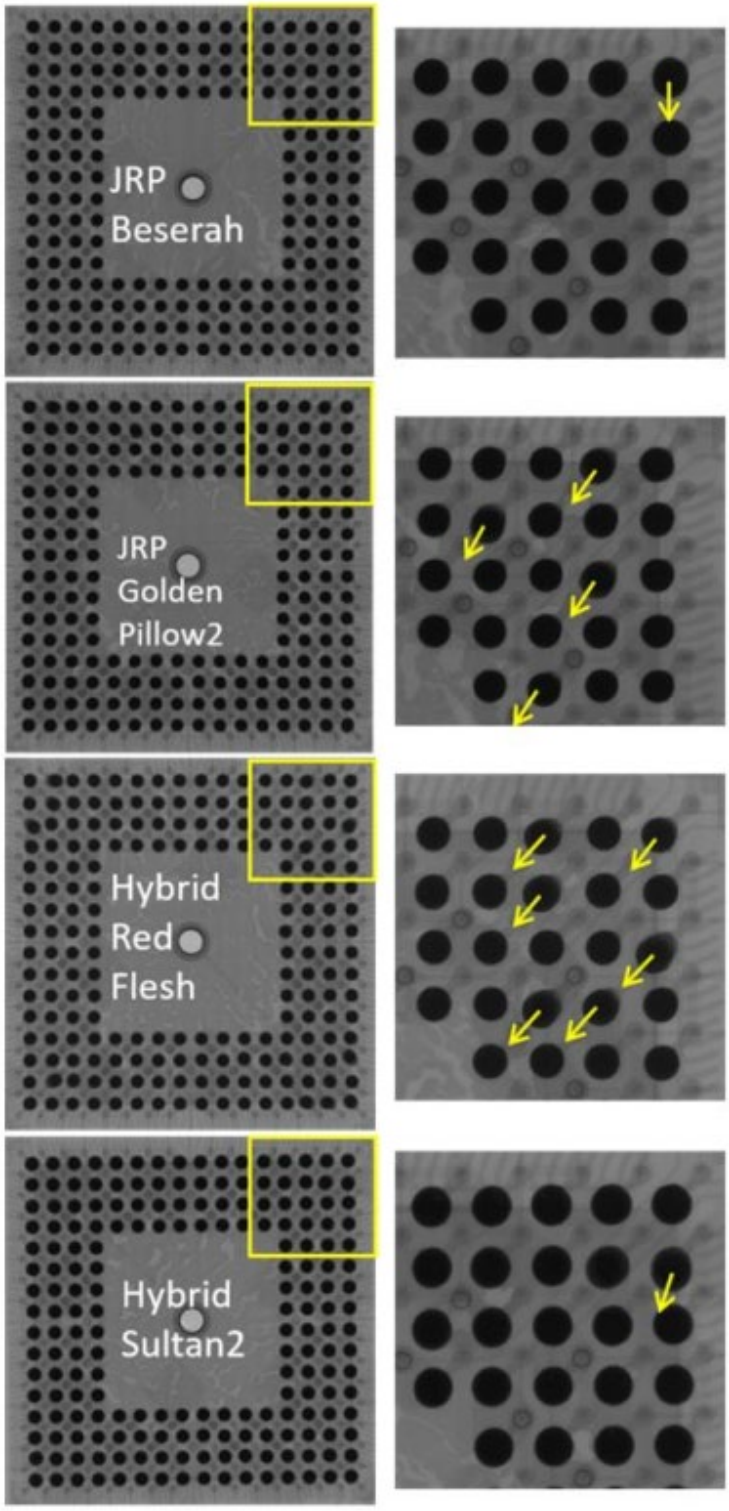

Note: The 0/100 °C thermal cycle profile x-ray ball drift images above were published previously [37]

Appendix C
X-ray Detection of Ball Drift in a CABGA192 (-15/85°C profile)